

Piecewise Deterministic Markov Processes for Bayesian Inference of PDE Coefficients

Leon Riccius^{1*}, Iuri B.C.M. Rocha¹, Joris Bierkens²,
Hanne Kekkonen², Frans P. van der Meer¹

¹Faculty of Civil Engineering and Geosciences, Delft University of Technology, Stevinweg 1, Delft, 2628 CN, The Netherlands.

²Delft Institute of Applied Mathematics, Delft University of Technology, Mekelweg 4, Delft, 2628 CD, The Netherlands.

*Corresponding author(s). E-mail(s): l.f.riccius@tudelft.nl;
Contributing authors: i.rocha@tudelft.nl; joris.bierkens@tudelft.nl;
h.n.kekkonen@tudelft.nl; f.p.vandermeer@tudelft.nl;

Abstract

We develop a general framework for piecewise deterministic Markov process (PDMP) samplers that enables efficient Bayesian inference in non-linear inverse problems with expensive likelihoods. The key ingredient is a surrogate-assisted thinning scheme in which a surrogate model provides a proposal event rate and a robust correction mechanism enforces an upper bound on the true rate by dynamically adjusting an additive offset whenever violations are detected. This construction is agnostic to the choice of surrogate and PDMP, and we demonstrate it for the Zig-Zag sampler and the Bouncy particle sampler with constant, Laplace, and Gaussian process (GP) surrogates, including gradient-informed and adaptively refined GP variants. As a representative application, we consider Bayesian inference of a spatially varying Young's modulus in a one-dimensional linear elasticity problem. Across dimensions, PDMP samplers equipped with GP-based surrogates achieve substantially higher accuracy and effective sample size per forward model evaluation than Random Walk Metropolis algorithm and the No-U-Turn sampler. The Bouncy particle sampler exhibits the most favorable overall efficiency and scaling, illustrating the potential of the proposed PDMP framework beyond this particular setting.

Keywords: Bayesian inference, Piecewise-deterministic Markov process, Zig-Zag sampler, Bouncy particle sampler, Markov chain Monte Carlo, Gaussian process regression, partial differential equations

1 Introduction

Markov chain Monte Carlo (MCMC) methods form a cornerstone of numerous scientific and engineering disciplines, including statistical physics, computational biology, and machine learning. These methods are widely used for sampling from complex, typically unnormalized probability distributions that frequently arise in these contexts. A particularly prominent application of MCMC is Bayesian inference, where samples are drawn from posterior distributions to quantify uncertainties in model parameters based on observed data.

The majority of established MCMC methods are built upon the Random Walk Metropolis (RWM) algorithm [1] and its generalization to non-symmetric proposals, the Metropolis-Hastings algorithm [2]. Despite their popularity due to simplicity and guaranteed asymptotic convergence, these algorithms suffer from poor sampling efficiency in high-dimensional parameter spaces due to their inherently diffusive nature [3]. To address these limitations, various advanced methods with improved sampling efficiency have emerged. Notable examples include the first-order Metropolis-adjusted Langevin algorithm [4], Hamiltonian Monte Carlo (HMC) [5], and their second-order manifold-aware extensions [6]. The No-U-Turn sampler (NUTS) [7] further enhances HMC by promoting large transitions without the need for manual tuning of trajectory lengths, and is widely adopted in probabilistic programming frameworks such as Stan [8] and PyMC [9]. Empirical evaluations of these methods on practical engineering problems [6, 10, 11] confirm that their theoretically superior convergence properties observed on canonical test distributions [12, 13] often carry over to realistic engineering applications.

All aforementioned methods share a common characteristic: reversibility. Specifically, they satisfy the detailed balance condition, which ensures convergence to the target distribution but limits their sampling efficiency due to diffusive dynamics [14, ch 6.1]. Recently, there has been growing interest in irreversible sampling algorithms, motivated by theoretical results demonstrating their potential for faster convergence and lower asymptotic variance [15, 16].

Irreversible algorithms can be broadly categorized into two types. One approach involves lifting reversible algorithms onto higher-dimensional state spaces [17]. The second approach relies on piecewise deterministic Markov processes (PDMPs). PDMP-based samplers include the Zig-Zag sampler [18], the Bouncy Particle sampler [19], and the Boomerang sampler [20]. These samplers evolve deterministically and are occasionally interrupted by stochastic events that abruptly alter their trajectories. While these algorithms have favorable theoretical properties, such as good mixing, low autocorrelation, and error-free subsampling [21], their simulation is prohibitively expensive beyond a few simple examples of academic nature. To date, PDMP samplers have only seen limited application to practical problems, e.g. linear Bayesian inverse problems [22].

The PDMP samplers define a non-homogeneous Poisson process. In such a process, the time until next event is exponentially distributed with a rate that depends on the current state and the gradient of the log-density of interest. A direct simulation of the next event time involves solving an integral equation, which has a closed form only for a few simple distributions, such as the Gaussian distribution with its quadratic

log-density. For more complex distributions, the next event time can be obtained via numerical integration of the event rate. In [23], the Zig-Zag sampler and Bouncy particle sampler are discretized with a forward Euler scheme, essentially defining a Markov chain on a grid of states. Higher-order discretizations were considered in [24]. While numerical integration opens PDMP sampling to a wide range of distributions, it is still not competitive in terms of computational cost in most cases.

The events can also be generated indirectly via Poisson thinning [21]. The thinning is applicable if an upper bound process is available, i.e. a Poisson process with a rate strictly higher than the one of the process of interest. A candidate event generated from this upper bound process is accepted with a probability equal to the ratio of the true rate and the upper bound. Poisson thinning is only viable if events from the upper bound process can be generated efficiently. In [25], a constant upper bound for a given time horizon is found by a polynomial fit to the switching rate of the Zig-Zag sampler. This process is repeated for each new state.

The direct inversion, as well as the thinning in [25] can be summarized as purely local approaches for simulating PDMPs, as they only consider the log-density and the event rate in the vicinity of the current state. In this work, we propose a more global approach to PDMP simulation, attempting to find an approximation of the event rate that can be used throughout the domain. In theory, the event rate along the trajectory of the PDMP is sufficient to generate the next event. In practice, the information about the event rate in the rest of the domain can aid this event generation.

Our approach uses surrogate models to construct proposal rates for Poisson thinning for approximate PDMP sampling. A key feature is a correction mechanism that dynamically adjusts the surrogate whenever a violation of the upper bound condition is detected during simulation. This correction mechanism renders the thinning procedure agnostic to the specific surrogate used: the only requirement is that the surrogate induces a computable proposal rate. This flexibility allows us to explore a range of surrogate families—from simple constant potentials or Laplace approximations to more expressive GP models—and to devise adaptive versions that incorporate information from the sampling process itself.

Our approach is tailored to unimodal, smooth posterior distributions defined on continuous parameter spaces. Such distributions typically arise in the context of elliptic partial differential equations (PDEs)—e.g. heat conduction, electrostatics, or diffusion—and the inference of their coefficients. We demonstrate and test our method on a simple yet illustrative example problem in linear elasticity, where we infer parameter fields from noisy displacement observations. Our method is agnostic to the specific choice of PDMP sampler. We apply it to both the Zig-Zag sampler and the Bouncy particle sampler and compare their performance. Both samplers outperform a well-tuned RWM baseline and the popular NUTS across all considered metrics and settings, marking a step towards greater application of PDMP sampling in Bayesian inference.

The remainder of this work is structured as follows. In Section 2, we review the foundations of PDMP sampling. Section 3 introduces our surrogate-assisted PDMP sampling framework and the surrogate model choices. In Section 4, we present numerical experiments demonstrating the performance of our method on a PDE-governed Bayesian inverse problem. Finally, Section 5 concludes the work with a summary and outlook on future research directions.

2 Piecewise-Deterministic Markov Process Samplers

PDMPs are continuous-time Markov processes characterized by deterministic trajectories interrupted by random events. We limit ourselves to PDMPs designed for sampling from a target distribution $\pi(\mathbf{x}) \propto \exp(-\Psi(\mathbf{x}))$ on $\mathcal{X} = \mathbb{R}^d$, where $\Psi : \mathbb{R}^d \rightarrow \mathbb{R}$ is a continuously differentiable potential. A widely used subclass of PDMP samplers, including the Zig-Zag and Bouncy particle samplers, is obtained by augmenting the position variable $\mathbf{x}_t \in \mathcal{X}$ with a velocity variable $\mathbf{v}_t \in \mathcal{V} = \mathbb{R}^d$. Following [26], a PDMP is defined by these three components:

1. *The deterministic dynamics:* Between events, the position $\mathbf{x}_t \in \mathcal{X} = \mathbb{R}^d$ and velocity $\mathbf{v}_t \in \mathcal{V} = \mathbb{R}^d$ evolve deterministically according to

$$\frac{d\mathbf{x}_t}{dt} = \Phi_{\mathbf{x}}(\mathbf{x}_t, \mathbf{v}_t), \quad \frac{d\mathbf{v}_t}{dt} = \Phi_{\mathbf{v}}(\mathbf{x}_t, \mathbf{v}_t), \quad (1)$$

where $\Phi_{\mathbf{x}}$ and $\Phi_{\mathbf{v}}$ are vector fields governing the evolution.

2. *The event rate:* At switching times τ , the PDMP undergoes a sudden transition. These events happen according to an inhomogeneous Poisson process with state-dependent, non-negative rate $\lambda(\mathbf{x}_t, \mathbf{v}_t)$.
3. *The transition kernel:* When an event occurs, the PDMP transitions from $(\mathbf{x}_t, \mathbf{v}_t)$ to $(\mathbf{x}'_t, \mathbf{v}'_t)$ according to a transition kernel $q(\mathbf{x}'_t, \mathbf{v}'_t | \mathbf{x}_t, \mathbf{v}_t)$.

Different choices for $\Phi_{\mathbf{x}}$, $\Phi_{\mathbf{v}}$, λ , and q , together with an initial condition $(\mathbf{x}_0, \mathbf{v}_0)$, fully define the PDMP.

The Zig-Zag and Bouncy particle samplers feature piecewise constant velocities. Between events, the dynamics are

$$\frac{d\mathbf{x}_t}{dt} = \mathbf{v}_t, \quad \frac{d\mathbf{v}_t}{dt} = 0. \quad (2)$$

The position \mathbf{x}_{t+s} at time $t+s$ is straightforward in this case:

$$\mathbf{x}_{t+s} = \mathbf{x}_t + s \cdot \mathbf{v}_t. \quad (3)$$

We will drop the time subscript for brevity in the following when there is no ambiguity.

These simple dynamics allow us to represent the trajectory of the PDMP entirely in terms of a skeleton $\{(t^k, \mathbf{x}^k, \mathbf{v}^k)\}_{k \geq 0}$, which consists of event times t^k and the corresponding states $(\mathbf{x}^k, \mathbf{v}^k)$ immediately after each event. Using Eq. (3), any position \mathbf{x}_t at time $t \in [t^k, t^{k+1}]$ can then be linearly interpolated as $\mathbf{x}_t = \mathbf{x}^k + \mathbf{v}^k \cdot (t - t^k)$.

2.1 The Zig-Zag Sampler

The velocity space of the Zig-Zag sampler is discrete: $\mathcal{V} = \{-1, +1\}^d$. Events occur independently in each coordinate direction i with state-dependent intensity

$$\eta_i(\mathbf{x}, \mathbf{v}) = \max \left\{ 0, v_i \frac{\partial \Psi(\mathbf{x})}{\partial x_i} \right\}. \quad (4)$$

yielding a total event rate of

$$\lambda(\mathbf{x}, \mathbf{v}) = \sum_{i=1}^d \eta_i(\mathbf{x}, \mathbf{v}). \quad (5)$$

Events can be simulated from the total event rate (5). The component to be flipped can then be selected with probability p_i proportional to its event rate

$$p_i = \frac{\eta_i(\mathbf{x}, \mathbf{v})}{\lambda(\mathbf{x}, \mathbf{v})}. \quad (6)$$

Alternatively, the events can be simulated directly from the individual component rates. The next switching time τ is then given by the minimum of the switching times τ_i across all components,

$$\tau = \min_{i=1, \dots, d} \tau_i, \quad (7)$$

and the process moves forward to $\mathbf{x}' = \mathbf{x} + \tau \cdot \mathbf{v}$.

At the occurrence of an event, the transition kernel q flips the sign of a single component v_i of the velocity vector \mathbf{v} . The velocity right after the event \mathbf{v}' is given by

$$\begin{aligned} v'_i &= -v_i, \\ v'_j &= v_j \quad \forall j \neq i, \end{aligned} \quad (8)$$

which yields the transition kernel q :

$$q(\mathbf{v}' | \mathbf{x}', \mathbf{v}) = \delta(\mathbf{v} - 2\mathbf{e}_i \mathbf{e}_i^\top \mathbf{v}), \quad (9)$$

where \mathbf{e}_i is the i -th standard basis vector in \mathbb{R}^d . The position remains unchanged during the state update. This construction yields a process with stationary distribution $p(\mathbf{x}, \mathbf{v}) = p(\mathbf{x})p(\mathbf{v})$, where $p(\mathbf{v})$ is uniform over $\{-1, +1\}^d$ and $p(\mathbf{x}) = \pi(\mathbf{x})$. The Zig-Zag sampler is ergodic under mild conditions on the target distribution [27].

The movement of the Zig-Zag sampler is guided by the gradient of the potential function $\nabla \Psi(\mathbf{x})$. When the sampler moves towards regions of higher density (i.e. lower potential), the event rate is zero. However, when the sampler moves towards the tails of $\pi(\mathbf{x})$ (i.e. higher potential), the event rate increases, leading to a higher chance of encountering an event. Upon such an event, the respective velocity component flips, and the sampler is redirected back towards regions of higher density. The position, velocity, and the resulting component-wise event rates of two consecutive events of the Zig-Zag sampler on a two-dimensional Gaussian target are illustrated in Fig. 1.

2.2 The Bouncy Particle Sampler

The Bouncy particle sampler employs a continuous velocity space $\mathcal{V} = \mathbb{R}^d$. Upon an event, the velocity is reflected against a hyperplane tangential to an isocontour of the

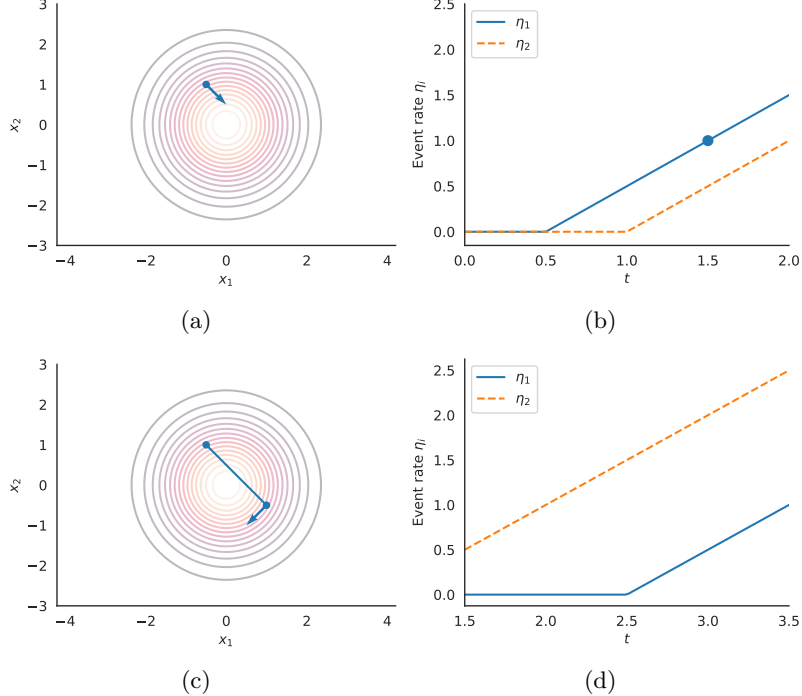


Fig. 1: Illustration of the Zig-Zag sampler on a two-dimensional Gaussian. Figures (a) and (c) show the target density with the current position (dot) and velocity (arrow). Figures (b) and (d) show the corresponding event rates along each coordinate direction.

target potential:

$$q(\mathbf{v}'|\mathbf{x}', \mathbf{v}) = \delta\left(\mathbf{v} - 2 \frac{\langle \mathbf{v}, \nabla \Psi(\mathbf{x}') \rangle}{\|\nabla \Psi(\mathbf{x}')\|^2} \nabla \Psi(\mathbf{x}')\right). \quad (10)$$

This reflection flips the component in the direction of the gradient of the potential, effectively returning the particle towards regions of higher probability density. Again, the position \mathbf{x} is unaffected by the event. The reflection events occur with state-dependent intensity

$$\lambda(\mathbf{x}, \mathbf{v}) = \max\{0, \langle \mathbf{v}, \nabla \Psi(\mathbf{x}) \rangle\}. \quad (11)$$

The bounce mechanism and event rate of the Bouncy particle sampler are illustrated on a two-dimensional Gaussian target in Fig. 2.

Because the original version of this algorithm [28] is not ergodic in certain scenarios, [19] introduced random refreshments to ensure this sampler can visit the entire state space. These random refreshment events, where the velocity is resampled from its stationary distribution $p(\mathbf{v}) = \mathcal{N}(\mathbf{0}, \mathbf{I})$, are exponentially distributed with rate $\lambda_{\text{ref}} > 0$. If λ_{ref} is too low, the sampler may struggle to reach certain regions of the state space.

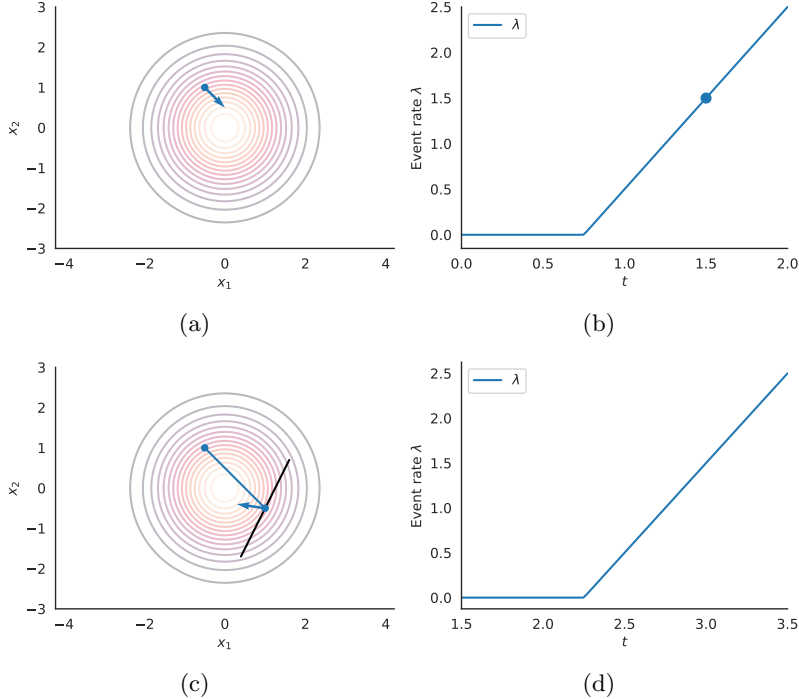


Fig. 2: Illustration of the Bouncy particle sampler on a two-dimensional Gaussian. Figures (a) and (c) show the target density with the current position (dot) and velocity (arrow). Figures (b) and (d) show the resulting event rate. Note that the event rate remains zero for longer, but has a steeper slope than in the Zig-Zag sampler.

If λ_{ref} is too high, the sampler may exhibit diffusive behaviour, reducing its efficiency. The optimal choice of λ_{ref} is problem-dependent and often requires empirical tuning.

The Bouncy particle sampler can in theory find better paths through the state space on isotropic targets due to its continuous velocity space [29]. However, one needs to carefully tune the refreshment rate λ_{ref} to ensure ergodicity. The Zig-Zag sampler, on the other hand, does not require such tuning and runs out-of-the-box for a wide range of targets.

2.3 Simulating Events with Poisson Thinning

Simulating event times from an inhomogeneous Poisson process with rate function $\lambda(\mathbf{x}_t, \mathbf{v}_t)$ can be challenging. Two common methods for simulating these event times are the inverse method and the thinning algorithm (both described in [30]). The inverse method involves computing the integrated rate function

$$\Lambda(t) = \int_0^t \lambda(\mathbf{x}_s, \mathbf{v}_s) ds, \quad (12)$$

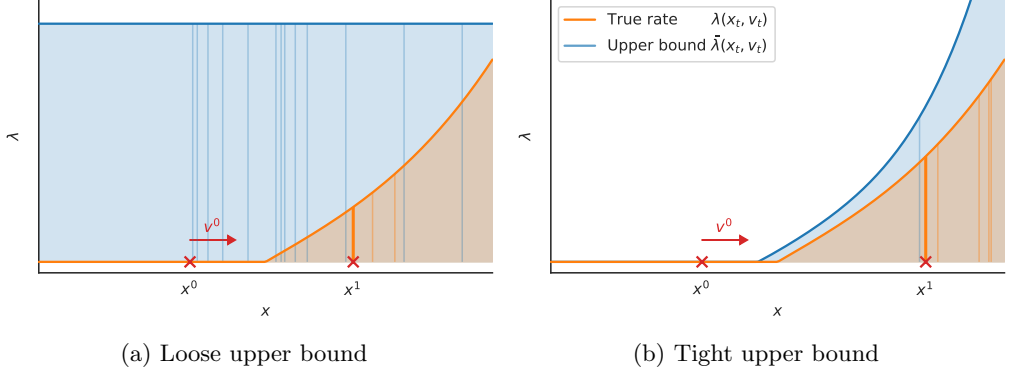


Fig. 3: Illustration of the thinning procedure for simulating event times. The vertical lines represent candidate event times drawn from a Poisson process with upper bound $\bar{\lambda}$. Rejected events are shown in blue, while accepted events are shown in orange. Fewer rejections is better.

and then sampling the next event time τ by solving

$$\Lambda(\tau) = -\log u, \quad (13)$$

where $u \sim \mathcal{U}(0, 1)$. This method requires that the integrated rate function $\Lambda(t)$ can be computed and inverted efficiently, which is generally not the case for non-linear PDE-governed Bayesian inverse problems.

The thinning algorithm provides an alternative approach that does not require the inversion of the integrated rate function. It involves simulating a candidate switching time τ from a Poisson process with an upper bound $\bar{\lambda}$ on the rate function λ . The candidate switching time τ is accepted with probability

$$a(\tau) = \frac{\lambda(\mathbf{x}_{t+\tau}, \mathbf{v}_{t+\tau})}{\bar{\lambda}(\mathbf{x}_{t+\tau}, \mathbf{v}_{t+\tau})}. \quad (14)$$

If the candidate is rejected, we restart the event generation from time $t + \tau$ without updating the velocity.

The thinning procedure is illustrated in Fig. 3 with a loose (left) and a tight (right) upper bound $\bar{\lambda}$. A tighter the upper bound, such as in Fig. 3b, yields a more efficient algorithm, as fewer candidate events will be rejected. As Eq. (14) must be evaluated for each candidate event, having a smaller number of rejections is particularly attractive when each evaluation of the true event rate λ is computationally expensive, e.g. solving a PDE for a realization of the parameter vector.

2.4 Affine Transformation

Both the Zig-Zag sampler and the Bouncy particle sampler preserve their target distribution under affine reparameterizations of the state space [23]. More precisely, let

$$\boldsymbol{\xi} = \mathbf{A}^{-1}(\mathbf{x} - \mathbf{b}), \quad (15)$$

for some invertible matrix $\mathbf{A} \in \mathbb{R}^{d \times d}$ and vector $\mathbf{b} \in \mathbb{R}^d$. Running the Zig-Zag sampler or Bouncy particle sampler in the $\boldsymbol{\xi}$ -coordinates with the transformed density

$$\tilde{\pi}(\boldsymbol{\xi}) \propto \pi(\mathbf{A}\boldsymbol{\xi} + \mathbf{b}) \quad (16)$$

and then mapping the resulting trajectory back via

$$\mathbf{x} = \mathbf{A}\boldsymbol{\xi} + \mathbf{b}, \quad (17)$$

yields a process in the original coordinates whose invariant distribution is $\pi(\mathbf{x})$. This affine equivariance property may be exploited to improve sampling efficiency on anisotropic posterior distributions [29].

In practice, we construct a local preconditioning transformation based on a Laplace approximation. Let \mathbf{x}_{MAP} denote the maximum a posteriori estimate and let $\mathbf{H} = \nabla^2\Psi(\mathbf{x}_{\text{MAP}})$ be the Hessian of the potential at that point. We compute the Cholesky factorization $\mathbf{H} = \mathbf{L}\mathbf{L}^T$ and define the affine change of variables

$$\boldsymbol{\xi} = \mathbf{L}^T(\mathbf{x} - \mathbf{x}_{\text{MAP}}), \quad (18)$$

or, equivalently, $\mathbf{x} = \mathbf{x}_{\text{MAP}} + \mathbf{L}^{-T}\boldsymbol{\xi}$, which centres the posterior at the MAP and locally whitens it with respect to the curvature of Ψ . The transformed potential is then

$$\tilde{\Psi}(\boldsymbol{\xi}) = \Psi(\mathbf{x}_{\text{MAP}} + \mathbf{L}^{-T}\boldsymbol{\xi}). \quad (19)$$

In the general mapping $\mathbf{x} = \mathbf{A}\boldsymbol{\xi} + \mathbf{b}$ above, this choice corresponds to $\mathbf{A} = \mathbf{L}^{-T}$ and $\mathbf{b} = \mathbf{x}_{\text{MAP}}$. We run the Zig-Zag sampler or Bouncy particle sampler in the transformed space with density proportional to $\exp(-\tilde{\Psi}(\boldsymbol{\xi}))$, obtaining a trajectory Ξ_t , and then map back via $\mathbf{x} = \mathbf{x}_{\text{MAP}} + \mathbf{L}^{-T}\boldsymbol{\xi}$.

3 Poisson Thinning with Surrogate Models

Thinning requires an upper bound on the true PDMP event rate. For the transformed potential $\tilde{\Psi}(\boldsymbol{\xi})$, this transformed rate takes the form $\tilde{\lambda}(\boldsymbol{\xi}, \mathbf{v})$. The main idea is to use a surrogate model $\bar{\Psi}(\boldsymbol{\xi})$ to approximate the transformed potential $\tilde{\Psi}(\boldsymbol{\xi})$. We can then approximate the gradients of the potential $\nabla\bar{\Psi}(\boldsymbol{\xi}) \approx \nabla\tilde{\Psi}(\boldsymbol{\xi})$ and the process rate $\bar{\lambda}(\boldsymbol{\xi}, \mathbf{v}) \approx \tilde{\lambda}(\boldsymbol{\xi}, \mathbf{v})$. The cost of evaluating the surrogate is often orders of magnitudes lower than the cost of evaluating the true potential in PDE-governed inverse problems. Hence, we can use the direct inversion method and solve Eq. (13) numerically to

produce event time candidates efficiently with the surrogate rate. We then thin these candidates against the true event rate $\tilde{\lambda}(\xi, \mathbf{v})$ to obtain valid event times for the PDMP.

In theory, the upper bound process must satisfy the global constraint

$$\bar{\lambda}(\xi, \mathbf{v}) \geq \tilde{\lambda}(\xi, \mathbf{v}), \quad (20)$$

for all (ξ, \mathbf{v}) , which guarantees the correctness of the thinning procedure. In addition, we want this upper bound process to be as tight as possible for an efficient thinning procedure.

In practice, it is challenging to construct surrogate models that are both tight and satisfy the constraint in Eq. (20) globally. We instead enforce the upper-bound condition only locally along the realized trajectory. This is sufficient for correctness because event times in PDMPs depend solely on the rate integrated along the current path. A similar route is taken in [25], where local constant bounds for the event rate are constructed for a given time horizon. We extend this idea by using global surrogate models that can adapt to the local behaviour of the potential function. To ensure the correctness of the thinning procedure, we introduce a correction mechanism that adjusts the approximate rate $\bar{\lambda}$ whenever a violation of the upper bound condition is detected during the simulation.

Assuming that we violated the upper bound condition at some time t^k with position ξ^k with velocity \mathbf{v}^k , i.e. $\bar{\lambda}(\xi^k, \mathbf{v}^k) < \tilde{\lambda}(\xi^k, \mathbf{v}^k)$, we can correct the surrogate model locally by adding an offset γ to the event rate. Formally, we define the corrected event rate as

$$\bar{\lambda}^c(\xi, \mathbf{v}) = \max\{0, \langle \mathbf{v}, \nabla \bar{\Psi}(\xi) \rangle + \gamma\}, \quad (21)$$

for the Bouncy particle sampler. We initialize the offset to $\gamma = 0$ at the start of the simulation. In case of a violation of Eq. (20) at (ξ^k, \mathbf{v}^k) , we increase the offset γ as much as needed to satisfy the upper bound condition at the associated state:

$$\gamma = \max\{0, \tilde{\lambda}(\xi^k, \mathbf{v}^k) - \bar{\lambda}(\xi^k, \mathbf{v}^k)\}. \quad (22)$$

The Zig-Zag sampler is equipped with a vectorial offset $\gamma \in \mathbb{R}^d$, with components updated similarly to the scalar offset in the Bouncy particle sampler, exploiting the additive structure of the Zig-Zag sampler event rate:

$$\bar{\eta}_i^c(\xi, \mathbf{v}) = \max\left\{0, v_i \frac{\partial \bar{\Psi}(\xi)}{\partial \xi_i} + \gamma_i\right\}, \quad (23)$$

$$\bar{\lambda}^c(\xi, \mathbf{v}) = \sum_{i=1}^d \bar{\eta}_i^c(\xi, \mathbf{v}), \quad (24)$$

$$\gamma_i = \max\{0, \tilde{\eta}_i(\xi^k, \mathbf{v}^k) - \bar{\eta}_i^c(\xi^k, \mathbf{v}^k)\}, \quad (25)$$

where $\bar{\eta}_i^c$ is the component-wise proposal rate induced by the surrogate $\bar{\Psi}$.

We revert the process to time t^{k-1} , as the event that triggered the correction was invalid. We then re-simulate the next event using either the corrected total event rate $\bar{\lambda}^c$ for the Bouncy particle sampler or its components $\bar{\eta}_i^c$ for the Zig-Zag sampler. Note

that we must also re-use the same outcome of the uniform random variable used for the candidate generation (see Eq. (13)). Otherwise, we incur a bias towards sooner events, as these corrections occur more frequently when the PDMP travels further away from the mode of the target distribution. Such long traverses are more likely for larger outcomes of the uniform random variable u .

In its basic form, the offset γ increases over time, making the thinning procedure less efficient. To mitigate this issue, we implement a decay mechanism for the offset. Denoting γ^k the offset after the $(k-1)$ -th event occurring at time t^{k-1} , we obtain the offset γ^k that we use for the next interval $[t^k, t^{k+1})$ as

$$\gamma^k = \gamma^{k-1} \cdot \exp(-\beta(t^k - t^{k-1})), \quad (26)$$

which means the offset decays exponentially over time with rate $\beta > 0$. The discrete nature of the offset decay Eq. (26) means that the offset remains constant between events, and that we do not violate Eq. (20) when re-doing an event that triggered a correction. We note that even with this correction, there is still no guarantee that the upper bound condition Eq. (20) holds for all (ξ, v) along the trajectory, as we might miss fast oscillations of the rate between events. Our method is therefore approximate in nature. Section 4.3 holds a detailed discussion of the bias introduced by the approximate event generation scheme.

The complete algorithm for thinning with a corrected surrogate rate is detailed in Algorithm 1 for the Bouncy particle sampler. The counterpart for the Zig-Zag sampler is given in Algorithm 2. The Zig-Zag sampler version mainly differs in the way candidate event times are drawn and in the application of the correction mechanism. We apply the same decay to each component of the vectorial offset γ as we did for the scalar offset in the Bouncy particle sampler in Eq. (26). Both Algorithm 1 and Algorithm 2 return a skeleton of the trajectory, i.e. the sequence of event times and corresponding states $\{(t^k, \xi^k, v^k)\}_{k=0}^K$. We typically set a final time T and run the algorithms until $t_K \geq T$, as the PDMP samplers converge in terms of simulated time, not simulated events [27]. The full trajectory can then be reconstructed easily by linear interpolation between event times.

Algorithm 1 BPSWithSurrogate: scalar thinning with corrected surrogate rates

Require: approximate proposal rate $\bar{\lambda}(\xi, \mathbf{v})$; true rate $\tilde{\lambda}(\xi, \mathbf{v})$; initial state (ξ_0, \mathbf{v}_0) with $\mathbf{v}_0 \sim \mathcal{N}(\mathbf{0}, \mathbf{I})$; refresh rate $\lambda_{\text{ref}} > 0$; decay rate $\beta \geq 0$; end time T

Ensure: trajectory $\{(t^k, \xi^k, \mathbf{v}^k)\}_{k \geq 0}$

```

1:  $t \leftarrow 0$ ;  $(\xi, \mathbf{v}) \leftarrow (\xi_0, \mathbf{v}_0)$ ;  $k \leftarrow 0$ ;  $\gamma \leftarrow 0$ ;  $\Delta_t \leftarrow 0$ 
2: while  $t < T$  do
3:    $\gamma \leftarrow \gamma \exp(-\beta \Delta_t)$  ▷ discrete decay
4:    $\bar{\lambda}^c \leftarrow \max\{0, \langle \mathbf{v}, \nabla \bar{\Psi}(\xi) \rangle + \gamma\}$ 
5:   draw  $u_{\text{ref}} \sim \mathcal{U}(0, 1)$ ; set  $\tau_{\text{ref}} \leftarrow -\log u_{\text{ref}} / \lambda_{\text{ref}}$  ▷ refreshment clock
6:   draw  $u_b \sim \mathcal{U}(0, 1)$ ; find  $\tau_b \geq 0$  solving  $\int_0^{\tau_b} \bar{\lambda}^c(\xi + s \mathbf{v}, \mathbf{v}) ds = -\log u_b$  per Eq. (13); set  $\xi_p \leftarrow \xi + \tau_b \mathbf{v}$ ; set event  $\leftarrow$  bounce
7:   while true do ▷ correction loop reusing  $u_b$ 
8:     if  $\tau_b > \tau_{\text{ref}}$  then ▷ check refresh preemption
9:       event  $\leftarrow$  refresh; break
10:    end if
11:     $\Delta_\lambda \leftarrow \tilde{\lambda}(\xi_p, \mathbf{v}) - \bar{\lambda}^c(\xi_p, \mathbf{v})$ 
12:    if  $\Delta_\lambda < 0$  then
13:      break ▷ valid bounce candidate under bound
14:    else
15:       $\gamma \leftarrow \gamma + \Delta_\lambda$ ;  $\bar{\lambda}^c \leftarrow \max\{0, \langle \mathbf{v}, \nabla \bar{\Psi}(\xi) \rangle + \gamma\}$ 
16:      recompute  $\tau_b$  by solving  $\int_0^{\tau_b} \bar{\lambda}^c(\xi + s \mathbf{v}, \mathbf{v}) ds = -\log u_b$ 
17:      set  $\xi_p \leftarrow \xi + \tau_b \mathbf{v}$ 
18:    end if
19:  end while
20:  if event is refresh then
21:     $t \leftarrow t + \tau_{\text{ref}}$ ;  $\xi \leftarrow \xi + \tau_{\text{ref}} \mathbf{v}$ ;  $\Delta_t \leftarrow \tau_{\text{ref}}$ 
22:    resample  $\mathbf{v} \sim \mathcal{N}(\mathbf{0}, \mathbf{I})$  ▷ refreshment
23:    continue
24:     $k \leftarrow k + 1$ ;  $t^k \leftarrow t$ ;  $\xi^k \leftarrow \xi$ ;  $\mathbf{v}^k \leftarrow \mathbf{v}$ 
25:  else
26:     $t \leftarrow t + \tau_b$ ;  $\xi \leftarrow \xi_p$ ;  $\Delta_t = \tau_b$ 
27:    if  $u_{\text{acc}} \leq \tilde{\lambda}(\xi_p, \mathbf{v}) / \bar{\lambda}^c(\xi_p, \mathbf{v})$  then ▷ accept bounce
28:      draw  $u_{\text{acc}} \sim \mathcal{U}(0, 1)$ 
29:      update  $\mathbf{v}$  by specular reflection per Eq. (10)
30:       $k \leftarrow k + 1$ ;  $t^k \leftarrow t$ ;  $\xi^k \leftarrow \xi$ ;  $\mathbf{v}^k \leftarrow \mathbf{v}$ ;
31:    end if
32:  end if
33: end while
34: return trajectory  $\{(t^k, \xi^k, \mathbf{v}^k)\}_{k \geq 0}$ 

```

Algorithm 2 ZZSWithSurrogate: component-wise thinning with corrected surrogate rates

Require: approximate potential $\bar{\Psi}(\xi)$; true component rates $\{\tilde{\eta}_i(\xi, v)\}_{i=1}^d$; initial state (ξ^0, v^0) with $v \in \{-1, +1\}^d$; decay rate $\beta \geq 0$; end time T

Ensure: trajectory $\{(t^k, \xi^k, v^k)\}_{k \geq 0}$

- 1: $t \leftarrow 0$; $(\xi, v) \leftarrow (\xi^0, v^0)$; $k \leftarrow 0$; $\Delta_t \leftarrow 0$
- 2: initialize vector offset $\gamma \leftarrow \mathbf{0} \in \mathbb{R}^d$
- 3: **while** $t < T$ **do**
- 4: $\gamma \leftarrow \gamma \exp(-\beta \Delta_t)$
- 5: $\bar{\eta}_i^c \leftarrow \max\{0, v_i \partial \bar{\Psi}(\xi) / \partial \xi_i + \gamma_i\}$ for $i = 1, \dots, d$
- 6: **for** $i = 1, \dots, d$ **do** ▷ draw independent candidate times
- 7: draw $u_i \sim \mathcal{U}(0, 1)$
- 8: find $\tau_i \geq 0$ solving $\int_0^{\tau_i} \bar{\eta}_i^c(\xi + s v, v) ds = -\log u_i$ per Eq. (13)
- 9: **end for**
- 10: **while** true **do** ▷ select earliest candidate; correct if bound violated
- 11: $i^* \leftarrow \arg \min_i \tau_i$; $\tau \leftarrow \tau_{i^*}$; $\xi_p \leftarrow \xi + \tau v$
- 12: $\Delta_\lambda \leftarrow \tilde{\eta}_{i^*}(\xi_p, v) - \bar{\eta}_{i^*}^c(\xi_p, v)$
- 13: **if** $\Delta_\lambda \leq 0$ **then**
- 14: **break** ▷ valid candidate under bound
- 15: **else**
- 16: $\gamma_{i^*} \leftarrow \gamma_{i^*} + \Delta_\lambda$; update $\bar{\eta}_{i^*}^c \leftarrow \max\{0, v_{i^*} \partial \bar{\Psi}(\xi) / \partial \xi_{i^*} + \gamma_{i^*}\}$
- 17: find τ_{i^*} solving $\int_0^{\tau_{i^*}} \bar{\eta}_{i^*}^c(\xi + s v, v) ds = -\log u_{i^*}$ ▷ reuse u_{i^*}
- 18: **end if**
- 19: **end while**
- 20: $t \leftarrow t + \tau$; $\xi \leftarrow \xi_p$; $\Delta_t \leftarrow \tau$
- 21: draw $u_{\text{acc}} \sim \mathcal{U}(0, 1)$
- 22: **if** $u_{\text{acc}} \leq \tilde{\eta}_{i^*}(\xi_p, v) / \bar{\eta}_{i^*}^c(\xi_p, v)$ **then** ▷ accept event
- 23: flip component i^* : $v_i \leftarrow -v_i$
- 24: $k \leftarrow k + 1$; $t^k \leftarrow t$; $\xi^k \leftarrow \xi$; $v^k \leftarrow v$
- 25: **end if**
- 26: **end while**
- 27: **return** trajectory $\{(t^k, \xi^k, v^k)\}_{k \geq 0}$

3.1 Surrogate-Agnostic Design and Surrogate Families

A key advantage of the correction mechanism is that it guarantees correctness regardless of the surrogate model. The only requirement is that the surrogate induces a computable proposal rate $\bar{\lambda}(\xi, v)$; whenever this is not an upper bound, the local offset γ in Eq. (21) restores correctness. Consequently, the approach works even with extremely crude surrogates. For example, taking a constant potential $\bar{\Psi}(\xi) \equiv c$ yields $\nabla \bar{\Psi} \equiv \mathbf{0}$ and thus an initial proposal rate of zero. In this case, we must initialize with a small non-zero offset (e.g. $\gamma = 1$) to generate candidate events from $\bar{\lambda}$; the first detected violation then raises the offset, after which the process proceeds correctly. While such a baseline will be inefficient—offsets grow quickly, thinning acceptance is low, frequent evaluation of $\tilde{\lambda}$ —it is valuable as a sanity check and lower-bound benchmark.

We consider the following surrogate families, ordered by increasing expressiveness and cost:

- Constant potential (baseline): $\bar{\Psi}(\xi) \equiv c$. No training; correctness entirely via offsets.
- Laplace (trivial in transformed coordinates): after the affine transformation, the Laplace model reduces to the standard normal potential, $\bar{\Psi}(\xi) = \frac{1}{2} \xi^\top \xi + c$, with gradient ξ and Hessian \mathbf{I} , and arbitrary constant c . This provides an inexpensive, stabilizing baseline around the mode.
- Laplace + GP residual: model the discrepancy $r(\xi) = \tilde{\Psi}(\xi) - \bar{\Psi}_L(\xi)$ with a GP-pre-trained on N_0 realizations of $r(\xi)$. This combined model captures non-quadratic structure while preserving good local behaviour.
- Laplace + GP with gradient observations: enrich the GP training set with gradients of $\tilde{\Psi}$ where available, using derivative kernels.
- Adaptive GP (thinning-driven): start with N_0 initial training points and expand the training set at milestone sizes $N_0 2^n$ for $n = 1, \dots, 5$, using data gathered from the thinning/simulation (e.g., locations of corrections or along accepted paths). This progressively tightens local rate proposals.

While we acknowledge the vast body of literature on more elaborate active learning schemes for GPs, we use the simple heuristic of the Adaptive GP model to demonstrate the potential of adaptive surrogates in this context. Here, we include *all* data gathered during simulation to expand the training set. We therefore treat this model as an upper performance bound for active learning.

We follow a simple, consistent pipeline across surrogates: first, we apply the affine transformation of Section 2.4 to whiten the state so that the Laplace approximation is standard normal in the transformed coordinate, as described in Algorithm 3. In these coordinates, the Laplace potential is trivial: $\bar{\Psi}_L = \frac{1}{2} \xi^\top \xi + c$, with gradient $\nabla \bar{\Psi}_L(\xi) = \xi$ and Hessian $\nabla^2 \bar{\Psi}_L(\xi) = \mathbf{I}$, see Algorithm 4. For all GP-based surrogates, we initialize by drawing N_0 samples $\{\xi_i\}_{i=1}^{N_0} \sim \mathcal{N}(\mathbf{0}, \mathbf{I})$, evaluating $\tilde{\Psi}(\xi_i)$, and training a GP on residuals $r(\xi_i) = \tilde{\Psi}(\xi_i) - \bar{\Psi}_L(\xi_i)$, as in Algorithm 5. for the gradient-observing variant, we additionally include derivative observations $\nabla r(\xi_i) = \nabla \tilde{\Psi}(\xi_i) - \nabla \bar{\Psi}_L(\xi_i)$. For the adaptive, the GP hyperparameters are updated at each milestone, as long as the total number of data points does not exceed 1000, as the computational costs grows cubically with the number of data points and further improvements are expected to be small in this data regime.

Algorithm 3 ComputeAffineTransformation: affine transform to whiten the Laplace approximation

Require: target potential $\Psi(\mathbf{x})$; initial guess $\mathbf{x}^{(0)}$; tolerance ε
Ensure: MAP estimate \mathbf{x}_{MAP} and Cholesky factor \mathbf{L} such that $\mathbf{H} = \mathbf{L}\mathbf{L}^T = \nabla^2\Psi(\mathbf{x}_{\text{MAP}})$; transformed coordinate is $\boldsymbol{\xi} = \mathbf{L}^T(\mathbf{x} - \mathbf{x}_{\text{MAP}})$ as in Section 2.4

- 1: Find $\mathbf{x}_{\text{MAP}} \leftarrow \arg \min_{\mathbf{x}} \Psi(\mathbf{x})$ using a gradient-based optimizer (e.g., SciPy BFGS) starting at $\mathbf{x}^{(0)}$; stop when $\|\nabla\Psi(\mathbf{x})\| < \varepsilon$
- 2: Compute analytic Hessian at the mode: $\mathbf{H} \leftarrow \nabla^2\Psi(\mathbf{x}_{\text{MAP}})$
- 3: Cholesky factorization: $\mathbf{H} = \mathbf{L}\mathbf{L}^T$
- 4: **return** $\mathbf{x}_{\text{MAP}}, \mathbf{L}$

Algorithm 4 BuildLaplaceSurrogate: quadratic surrogate in transformed coordinates

Require: target potential $\Psi(\mathbf{x})$; settings for Algorithm 3
Ensure: Laplace surrogate $\bar{\Psi}_L(\boldsymbol{\xi})$ in $\boldsymbol{\xi}$ -space; gradient $\nabla\bar{\Psi}_L(\boldsymbol{\xi})$; parameters $\mathbf{x}_{\text{MAP}}, \mathbf{L}$

- 1: $\mathbf{x}_{\text{MAP}}, \mathbf{L} \leftarrow \text{COMPUTEAFFINETRANSFORMATION}(\Psi)$ ▷ Algorithm 3
- 2: Define the transformed potential implicitly by $\tilde{\Psi}(\boldsymbol{\xi}) := \Psi(\mathbf{x}_{\text{MAP}} + \mathbf{L}^{-T}\boldsymbol{\xi})$
- 3: Define $\bar{\Psi}_L(\boldsymbol{\xi}) \leftarrow \frac{1}{2}\boldsymbol{\xi}^T\boldsymbol{\xi} + \tilde{\Psi}(\mathbf{0})$
- 4: Define $\nabla\bar{\Psi}_L(\boldsymbol{\xi}) \leftarrow \boldsymbol{\xi}$
- 5: **return** $\bar{\Psi}_L, \nabla\bar{\Psi}_L, \mathbf{x}_{\text{MAP}}, \mathbf{L}$

Algorithm 5 TrainGPSurrogate: GP residual on top of Laplace in transformed coordinates

Require: target potential $\Psi(\mathbf{x})$; initial design size N_0 ; kernel k_ϑ with init $\boldsymbol{\vartheta}^{(0)}$; includeGrad $\in \{\text{true}, \text{false}\}$
Ensure: surrogate mean $\bar{\Psi}_{\text{GP}}(\boldsymbol{\xi}) = \bar{\Psi}_L(\boldsymbol{\xi}) + m(\boldsymbol{\xi})$ with gradient; parameters $\mathbf{x}_{\text{MAP}}, \mathbf{L}$

- 1: $\bar{\Psi}_L, \nabla\bar{\Psi}_L, \mathbf{x}_{\text{MAP}}, \mathbf{L} \leftarrow \text{BUILDLAPLACESURROGATE}(\Psi)$ ▷ Algorithm 4
- 2: Draw $\{\boldsymbol{\xi}_i\}_{i=1}^{N_0} \sim \mathcal{N}(\mathbf{0}, \mathbf{I})$ ▷ training inputs in transformed space
- 3: **for** $i = 1, \dots, N_0$ **do**
- 4: $r_i \leftarrow r(\boldsymbol{\xi}_i) := \tilde{\Psi}(\boldsymbol{\xi}_i) - \bar{\Psi}_L(\boldsymbol{\xi}_i)$ ▷ residual in transformed coords
- 5: **if** includeGrad **then**
- 6: $\mathbf{g}_{\boldsymbol{\xi},i} \leftarrow \nabla_{\boldsymbol{\xi}}\tilde{\Psi}(\boldsymbol{\xi}_i)$ ▷ gradient in transformed coords via chain
- 7: $\mathbf{g}_i \leftarrow \mathbf{g}_{\boldsymbol{\xi},i} - \nabla\bar{\Psi}_L(\boldsymbol{\xi}_i)$ ▷ residual gradient
- 8: **end if**
- 9: **end for**
- 10: Assemble dataset $\mathcal{D} = \{(\boldsymbol{\xi}_i, r_i)\}$ (and gradient residuals if available)
- 11: Fit GP prior $f \sim \mathcal{GP}(0, k_\vartheta)$ by maximizing $\mathcal{L}(\boldsymbol{\vartheta})$ (33);
- 12: Define $m(\boldsymbol{\xi}) \leftarrow \mathbb{E}[f(\boldsymbol{\xi}) \mid \mathcal{D}, \hat{\boldsymbol{\vartheta}}]$ and $\nabla m(\boldsymbol{\xi})$ via (30)
- 13: Define composite surrogate $\bar{\Psi}_{\text{GP}}(\boldsymbol{\xi}) = \bar{\Psi}_L(\boldsymbol{\xi}) + m(\boldsymbol{\xi})$ with $\nabla\bar{\Psi}_{\text{GP}}(\boldsymbol{\xi}) = \nabla\bar{\Psi}_L(\boldsymbol{\xi}) + \nabla m(\boldsymbol{\xi})$
- 14: **return** $\bar{\Psi}_{\text{GP}}, \nabla\bar{\Psi}_{\text{GP}}, \mathbf{x}_{\text{MAP}}, \mathbf{L}$

3.2 Gaussian Process Surrogate

We model a smooth scalar function on the transformed coordinates in the residual $r(\boldsymbol{\xi}) = \tilde{\Psi}(\boldsymbol{\xi}) - \bar{\Psi}_L(\boldsymbol{\xi})$ with a GP. Let $\{(\boldsymbol{\xi}_i, y_i)\}_{i=1}^N$ denote training inputs and observations, where $y_i = f(\boldsymbol{\xi}_i) + \epsilon_i$ with independent noise $\epsilon_i \sim \mathcal{N}(0, \sigma_n^2)$. We place a constant-mean¹ GP prior $f \sim \mathcal{GP}(m, k_\vartheta)$. Let $\boldsymbol{\xi}, \boldsymbol{\xi}' \in \mathbb{R}^d$ denote two input locations. We use the anisotropic squared-exponential kernel

$$k_\vartheta(\boldsymbol{\xi}, \boldsymbol{\xi}') = \sigma_f^2 \exp\left(-\frac{1}{2} \sum_{j=1}^d \frac{(\xi_j - \xi'_j)^2}{\ell_j^2}\right), \quad \vartheta = \{m, \sigma_f^2, \ell_1, \dots, \ell_d, \sigma_n^2\}. \quad (27)$$

The diagonal, dimension-specific length-scales $\boldsymbol{\ell} = \{\ell_1, \dots, \ell_d\}$ reflect anisotropy, which is necessary as the affine transformation in Section 2.4 only whitens the target in the vicinity of the posterior mode. Together with the signal variance σ_f^2 , observation noise σ_n^2 , and mean parameter m , this yields $d + 3$ hyperparameters, with d being the dimensionality of $\boldsymbol{\xi}$.

We collect the kernel matrix $\mathbf{K} \in \mathbb{R}^{N \times N}$ with entries $[\mathbf{K}]_{ij} = k_\vartheta(\boldsymbol{\xi}_i, \boldsymbol{\xi}_j)$ and let $\mathbf{K}_y = \mathbf{K} + \sigma_n^2 \mathbf{I}$. For a test location $\boldsymbol{\xi}_*$, we define the cross-covariance vector $\mathbf{K}_* = [k_\vartheta(\boldsymbol{\xi}_*, \boldsymbol{\xi}_1), \dots, k_\vartheta(\boldsymbol{\xi}_*, \boldsymbol{\xi}_N)]^\top$ and the observations $\mathbf{y} = [y_1, \dots, y_N]^\top$. The GP posterior mean and variance are then:

$$m_*(\boldsymbol{\xi}_*) = m + \mathbf{K}_*^\top \mathbf{K}_y^{-1} (\mathbf{y} - m\mathbf{1}), \quad (28)$$

$$s_*^2(\boldsymbol{\xi}_*) = k_\vartheta(\boldsymbol{\xi}_*, \boldsymbol{\xi}_*) - \mathbf{K}_*^\top \mathbf{K}_y^{-1} \mathbf{K}_*, \quad (29)$$

We evaluate $m_*(\boldsymbol{\xi})$ as the surrogate mean and, when needed, its gradient to approximate the potential of the target distribution.

Gradients with respect to the input are available in closed form. Writing $\boldsymbol{\alpha} = \mathbf{K}_y^{-1}(\mathbf{y} - m\mathbf{1})$, the gradient of the predictive mean is

$$\nabla_{\boldsymbol{\xi}} m_*(\boldsymbol{\xi}) = \sum_{i=1}^N \alpha_i \nabla_{\boldsymbol{\xi}} k_\vartheta(\boldsymbol{\xi}, \boldsymbol{\xi}_i) \quad (30)$$

$$\nabla_{\boldsymbol{\xi}} k_\vartheta(\boldsymbol{\xi}, \boldsymbol{\xi}_i) = k_\vartheta(\boldsymbol{\xi}, \boldsymbol{\xi}_i) \text{diag}(\boldsymbol{\ell})^{-1}(\boldsymbol{\xi}_i - \boldsymbol{\xi}), \quad (31)$$

noting that the constant mean parameter m does not depend on $\boldsymbol{\xi}$ and hence does not contribute to $\nabla_{\boldsymbol{\xi}} m_*(\boldsymbol{\xi})$. If derivative observations are incorporated, we augment the GP with joint covariances obtained by differentiating the kernel: $\text{cov}(\partial_p f(\boldsymbol{\xi}), f(\boldsymbol{\xi}')) = \partial_{\boldsymbol{\xi}_p} k_\vartheta(\boldsymbol{\xi}, \boldsymbol{\xi}')$ and

$$\text{cov}(\partial_p f(\boldsymbol{\xi}), \partial_q f(\boldsymbol{\xi}')) = \partial_{\boldsymbol{\xi}_p} \partial_{\boldsymbol{\xi}'_q} k_\vartheta(\boldsymbol{\xi}, \boldsymbol{\xi}') = k_\vartheta(\boldsymbol{\xi}, \boldsymbol{\xi}') \left(\frac{\delta_{pq}}{\ell_p^2} - \frac{(\boldsymbol{\xi}_p - \boldsymbol{\xi}'_p)(\boldsymbol{\xi}_q - \boldsymbol{\xi}'_q)}{\ell_p^2 \ell_q^2} \right), \quad (32)$$

with δ_{pq} the Kronecker delta and ∂_p the derivative w.r.t. the p -th input dimension.

¹While the constant mean does not affect the gradients of the GP posterior mean, it can improve hyperparameter estimation and numerical stability [31].

Hyperparameter estimation proceeds by maximizing the marginal likelihood. The log marginal likelihood for ϑ is

$$\mathcal{L}(\vartheta) = \log p(\mathbf{y}|\boldsymbol{\xi}_1, \dots, \boldsymbol{\xi}_N, \vartheta) = -\frac{1}{2}(\mathbf{y} - m\mathbf{1})^\top \mathbf{K}_y^{-1}(\mathbf{y} - m\mathbf{1}) - \frac{1}{2} \log |\mathbf{K}_y| - \frac{N}{2} \log(2\pi), \quad (33)$$

In practice, we compute \mathcal{L} and its gradients via a Cholesky factorization $\mathbf{K}_y = \mathbf{L}\mathbf{L}^\top$, which yields $\boldsymbol{\alpha} = \mathbf{L}^{-\top}\mathbf{L}^{-1}(\mathbf{y} - m\mathbf{1})$ and $\log|\mathbf{K}_y| = 2 \sum_i \log(\mathbf{L}_{ii})$. The gradient with respect to kernel and noise hyperparameters takes the standard form

$$\frac{\partial \mathcal{L}}{\partial \vartheta_j} = \frac{1}{2} \text{tr} \left((\boldsymbol{\alpha}\boldsymbol{\alpha}^\top - \mathbf{K}_y^{-1}) \frac{\partial \mathbf{K}_y}{\partial \vartheta_j} \right), \quad (34)$$

with

$$\frac{\partial \mathbf{K}_y}{\partial \sigma_n^2} = \mathbf{I}, \quad (35)$$

and kernel-specific derivatives $\partial[\mathbf{K}_y]_{pq}/\partial \vartheta_j = \partial k_\vartheta(\boldsymbol{\xi}_p, \boldsymbol{\xi}_q)/\partial \vartheta_j$ with

$$\frac{\partial k_\vartheta(\boldsymbol{\xi}, \boldsymbol{\xi}')}{\partial \sigma_f^2} = \frac{k_\vartheta(\boldsymbol{\xi}, \boldsymbol{\xi}')}{\sigma_f^2}, \quad (36)$$

$$\frac{\partial k_\vartheta(\boldsymbol{\xi}, \boldsymbol{\xi}')}{\partial \ell_j} = k_\vartheta(\boldsymbol{\xi}, \boldsymbol{\xi}') \frac{(\xi_j - \xi'_j)^2}{\ell_j^3}. \quad (37)$$

The derivative with respect to the mean parameter is obtained from the quadratic term, $\partial \mathcal{L}/\partial m = \mathbf{1}^\top \mathbf{K}_y^{-1}(\mathbf{y} - m\mathbf{1})$.

4 Numerical Experiments

We begin by describing an experimental setup in Section 4.1, including a PDE problem, performance metrics, and implementation details. Focusing first on the Zig-Zag sampler, we analyse when the proposed surrogate-based thinning method yields correct convergence in Section 4.3. Section 4.4 then compares the different surrogate models, followed by an analysis of the adaptive GP version in Section 4.5. Finally, Section 4.6 benchmarks the Zig-Zag and Bouncy particle samplers against the No-U-Turn sampler [7].

4.1 Test Case

To demonstrate the proposed approach for PDMP sampling, we introduce a scalable case study. The problem is chosen to be computationally inexpensive, enabling direct comparison with long reference runs obtained using the Random-Walk Metropolis (RWM) algorithm. At the same time, the case study is motivated by its resemblance to practical engineering problems. Its nonlinear parameter-to-observable map leads to a non-Gaussian posterior distribution, well-suited to test the capabilities of the PDMP samplers and the surrogate-assisted framework.

Specifically, we consider the mechanical equilibrium of a one-dimensional linear elastic bar with a spatially varying and uncertain Young's modulus, which is to be

inferred from displacement measurements. The bar with length $L = 1$ and constant cross-sectional area $A = 1$ is depicted in Fig. 4.

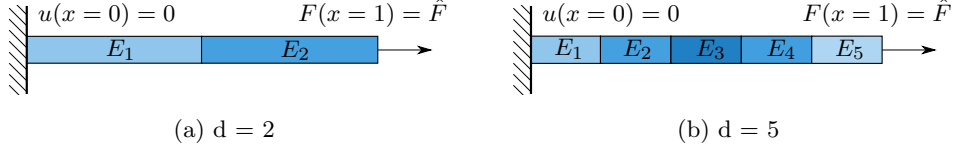


Fig. 4: Linear elastic bar problem with 2 and 5 dimensional discretization of Young's modulus field in (a) and (b), respectively.

The bar is fixed at the left end and subjected to a concentrated load $\hat{F} = 1$ at the right end. Assuming a linear elastic material, the displacement $u(x)$ along the bar is governed by the following boundary value problem:

$$\frac{d}{dx} \left(E(x) \frac{du(x)}{dx} \right) = 0, \quad x \in (0, 1), \quad (38)$$

$$u(0) = 0, \quad (39)$$

$$E(1) \frac{du(1)}{dx} = 1, \quad (40)$$

where the Young's modulus $E(x)$ depends on the position x . We consider this parameter field $E(x)$ to be uncertain. In many situations however, some prior knowledge about the parameter field is available.

Here we adopt a smooth, spatially correlated prior field, which we model as a log-Gaussian random field, owing to the positivity constraint of the Young's modulus. Such a field can be expressed as a Gaussian process:

$$\log E(x) \sim \mathcal{GP}(\mu_E(x), k_E(x, x')), \quad (41)$$

$$k_E(x, x') = \sigma_E^2 \exp\left(-\frac{(x - x')^2}{2l_E^2}\right). \quad (42)$$

Its three parameters are the mean function $\mu_E(x)$, the signal variance σ_E^2 , and the length scale l_E of the squared exponential covariance function $k_E(x, x')$. In practice, these parameters are estimated from data, e.g. using maximum likelihood estimation, set based on expert knowledge, or treated as hyperparameters in a hierarchical Bayesian model. For our testing purposes, we set $\mu_E = 1$, $\sigma_E = 1$ and $l_E = 0.3$, yielding a moderately varying field.

In theory, we would like to infer the continuous field $E(x)$. In practice, however, we need to discretize the field to represent it with a finite number of parameters θ . We

discretize the field with piecewise-constant basis functions ϕ_i

$$\log E(x; \boldsymbol{\theta}) = \sum_{i=1}^d \theta_i \phi_i x, \quad (43)$$

$$\phi_i(x) = \begin{cases} 1, & \text{if } \frac{i-1}{d} \leq x < \frac{i}{d}, \\ 0, & \text{elsewhere.} \end{cases} \quad (44)$$

leading to a parameter vector $\boldsymbol{\theta} \in \mathbb{R}^d$ of dimension d . We obtain the prior distribution of the parameters $p(\boldsymbol{\theta}) = \mathcal{N}(\mu_{\boldsymbol{\theta}}, \text{Cov}(\boldsymbol{\theta}))$ by projecting the Gaussian process onto the piecewise-constant basis functions. With $M_{ij} = \langle \phi_i, \phi_j \rangle$, the covariance matrix of the parameters $\boldsymbol{\theta}$ in the general case is given by

$$\text{Cov}(\theta_i, \theta_j) = \mathbf{M}^{-1} \int_0^1 \int_0^1 \phi_i(x) k_E(x, x') \phi_j(x') dx dx' \mathbf{M}^{-\top}. \quad (45)$$

(46)

Since the basis functions ϕ_i are non-overlapping, and the basis is orthogonal with $M_{ij} = 1/d \mathbf{I}$, the covariance simplifies to

$$\text{Cov}(\theta_i, \theta_j) = d^2 \int_{(i-1)/d}^{i/d} \int_{(j-1)/d}^{j/d} k_E(x, x') dx dx'. \quad (47)$$

With the constant mean function $\mu_E(x) = 1$ of the underlying process, the mean of the coefficients θ_i is given by

$$\mathbb{E}[\theta_i] = d \int_{(i-1)/d}^{i/d} E(x) dx = 1. \quad (48)$$

Together with the feature vector $\boldsymbol{\phi}(x) = [\phi_1(x), \dots, \phi_d(x)]^\top$, the covariance of the discretized logarithm of the parameter field is given by

$$\text{Cov}(\log E(x; \boldsymbol{\theta}), \log E(x'; \boldsymbol{\theta})) = \boldsymbol{\phi}(x)^\top \text{Cov}(\boldsymbol{\theta}) \boldsymbol{\phi}(x'), \quad (49)$$

which for $d \rightarrow \infty$ converges to the original covariance function $k_E(x, x')$ of the Gaussian process.

We acknowledge that the piecewise-constant basis functions are not ideal for representing a smooth Gaussian process. For most applications, other basis functions, such as Chebyshev polynomials or Karhunen-Loëve basis functions, would be more suitable. However, the piecewise-constant basis functions have a key advantage for our

testing purposes: they allow for an analytic solution of the forward problem, which reads

$$u(x; \boldsymbol{\theta}) = \left(\sum_{i=1}^{\lfloor xd \rfloor} \frac{\frac{1}{d}}{\exp \theta_i} + \frac{x - \lfloor xd \rfloor}{\exp \theta_{\lfloor xd \rfloor + 1}} \right), \quad x \in [0, 1]. \quad (50)$$

where $\lfloor \cdot \rfloor$ denotes the floor function. This solution is continuous and piecewise-linear, with kinks at the segment boundaries. Most notably, the displacements are a non-linear function of the latent variables $\boldsymbol{\theta}$, leading to a non-linear inverse problem. Due to the analytic solution, we can evaluate the forward model and run the inference at negligible computational cost, allowing us to focus on the analysis of the sampling algorithms themselves.

First, we draw a sample from the prior $\boldsymbol{\theta}^* \sim p(\boldsymbol{\theta})$ as the ground truth which we then try to infer from noisy displacement measurements $\tilde{\mathbf{u}}$. We generate these displacement measurements \tilde{u}_i by evaluating the forward model at m equidistant sensor locations $x_i = i/(m+1)$ for $i = 1, \dots, m$ and adding independent Gaussian noise with standard deviation $\sigma_{\text{obs}} = 0.025$. We therefore adopt a Gaussian likelihood model

$$p(\tilde{\mathbf{u}}|\boldsymbol{\theta}) = \mathcal{N}(\tilde{\mathbf{u}}|\mathbf{u}(\boldsymbol{\theta}), \sigma_{\text{obs}}^2 \mathbf{I}), \quad (51)$$

where $\tilde{\mathbf{u}} = [\tilde{u}_1, \dots, \tilde{u}_m]^\top$ are the noisy measurements, and $\mathbf{u}(\boldsymbol{\theta}) = [u(x_1; \boldsymbol{\theta}), \dots, u(x_m; \boldsymbol{\theta})]^\top$ are the model predictions at the sensor locations. Following [32], we set the number of sensors to $m = \lfloor 3/4d \rfloor$. Fixing the observation-to-parameters ratio in this manner helps to maintain a consistent level of problem difficulty across different parameter dimensions d .

Finally, we summarize the Bayesian inference problem as

$$p(\boldsymbol{\theta}|\tilde{\mathbf{u}}) \propto p(\tilde{\mathbf{u}}|\boldsymbol{\theta}) p(\boldsymbol{\theta}), \quad (52)$$

where the prior $p(\boldsymbol{\theta})$ is the Gaussian distribution derived above. We can now estimate the posterior distribution using the PDMP methods described in Section 2, i.e. $\pi(\boldsymbol{\theta}) = p(\boldsymbol{\theta}|\tilde{\mathbf{u}})$. The posterior for the two-dimensional case is visualized in Fig. 5.

4.2 Evaluation Metrics

First, we compute a reference solution for each setting $d = 2, \dots, 10$ using a long RWM run with 10^7 samples. Let μ_i^* and $\sigma_i^{2,*}$ denote the coordinate-wise posterior mean and variance of this reference posterior. For any method \mathcal{M} , let $\hat{\mu}_i^{(\mathcal{M})}$ and $\hat{\sigma}_i^{2,(\mathcal{M})}$ denote the corresponding estimates. We then evaluate the following metrics:

Posterior Mean Error:

$$\text{RMSE}_{\text{mean}}^{(\mathcal{M})} = \sqrt{\frac{1}{d} \sum_{i=1}^d (\hat{\mu}_i^{(\mathcal{M})} - \mu_i^*)^2} \quad (53)$$

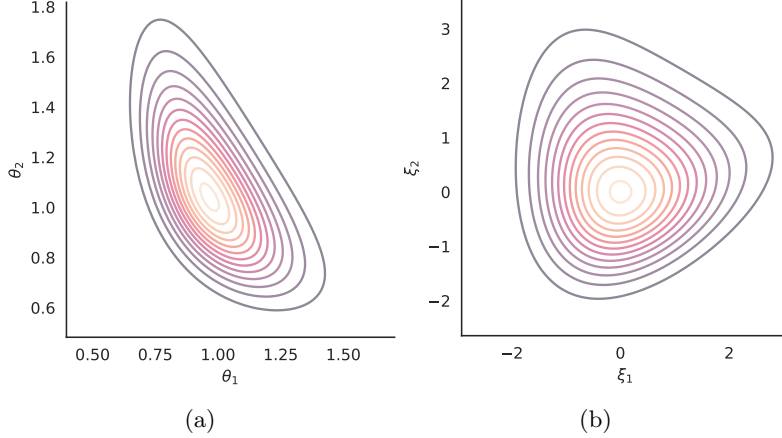


Fig. 5: Posterior distribution of the two-dimensional problem in the original (a) and the affine space (b).

Posterior Variance Error:

$$\text{RMSE}_{\text{var}}^{(\mathcal{M})} = \sqrt{\frac{1}{d} \sum_{i=1}^d (\hat{\sigma}_i^{2,(\mathcal{M})} - \sigma_i^{2,*})^2} \quad (54)$$

Wasserstein Distance: We compute the 2-Wasserstein distance (WD) between the reference solution \hat{p}^* and an approximation $\hat{p}^{(\mathcal{M})}$ resulting from method \mathcal{M} .

$$W_2^2(\hat{p}^*, \hat{p}^{(\mathcal{M})}) = \min_{\pi \in \Pi(\hat{p}^*, \hat{p}^{(\mathcal{M})})} \iint \|\xi - \xi'\|^2 d\pi(\xi, \xi') \quad (55)$$

where $\Pi(\hat{p}^*, \hat{p}^{(\mathcal{M})})$ denotes the set of all couplings of the two distributions.

Effective Sample Size (ESS) per Model Evaluation: We compute the ESS per model evaluation to assess the sampling efficiency of the PDMP methods. The ESS is calculated using the formula

$$\text{ESS} = \frac{N}{1 + 2 \sum_{k=1}^{\infty} \rho_k}, \quad (56)$$

where N is the total number of samples and ρ_k is the autocorrelation at lag k . We normalize the ESS by dividing it by the number of model evaluations N_{eval} to account for computational cost.

Remarks. We compute all metrics in the affine space to obtain standardized results. The posterior mean and variance of the PDMPs can be computed analytically, as shown in [27]. We display these quantities as functions of PDE model evaluations N_{eval} ,

as we assume these evaluations to be the computational bottleneck of our problem. This way, we can compare convergence of the different methods on equal footing. We therefore need to keep track of the number of model evaluations performed by the PDMP samplers. Markov chains are typically evaluated in terms of number of samples drawn, which is directly proportional to the number of model evaluations for the RWM sampler.

In [27], a method to compute the ESS directly from the PDMP skeleton without a need to discretize is also provided. However, we observe in the shorter runs considered here that the ESS computed from the discretized process produces more stable and accurate results. We therefore approximate the PDMP until time T and discretize it into N samples equally spaced in time, i.e. $\xi_i = \xi(i \cdot T/N)$ for $i = 1, \dots, N$.

In a similar manner, we discretize the PDMPs for the empirical WD, as no analytical solution for this metric is available. The exact empirical WD becomes prohibitively expensive to compute for large sample sizes and dimensions. We therefore resort to the debiased Sinkhorn divergence, as described in [33], as an efficient approximation. We set regularization parameter $\varepsilon = 0.02$ for numerical stability while keeping the bias low.

The WD is also reported as a function of model evaluations, similar to the posterior mean and variance. The empirical WD is a biased and noisy estimator of the true WD between the PDMP and the reference posterior, especially for small sample sizes. We do not correct for the bias in our experiments, but ensure comparability by using the same number of samples for all methods. This means that we discretize the PDMPs with N points when computing the WD distance after N model evaluations. We reduce the variance by taking multiple random draws of N samples from the reference posterior.

We repeat each numerical experiment 50 times with 50 different seeds, and then report the average for each of the four metrics. For each seed, the initial position of the sampling algorithm is drawn from the Laplace approximation of the posterior. Note that we run the MCMC algorithms in the affine space as well to put all algorithms on an equal footing. This way, we expect a short burn-in phase regardless of the algorithm. We obtain the affine transformation only once per setting and use it for all methods and seeds.

We provide a RWM baseline for all experiments, which is not to be confused with the reference solution with 10^7 samples. It is well known that the performance of RWM depends heavily on the choice of the proposal distribution. We start out with a standard Gaussian proposal, reflecting the isotropic nature of the posterior in the affine space. After each 100 iterations, we multiply the current proposal covariance with 0.9 if the acceptance rate is below 0.2, and with 1.1 if the acceptance rate is above 0.25. After 1000 iterations, we set the proposal covariance matrix to the empirical covariance of the samples collected so far, scaled by the optimal factor $2.38^2/d$ derived in [12]. We then keep rescaling the proposal covariance every 100 iterations as before, and leave it unchanged after 2000 iterations to satisfy vanishing adaptation [34]. It is also this version of the RWM algorithm that we use to compute the reference solutions, albeit with a different seed and a much longer run where we discard the first 5000 samples as burnin.

4.3 Convergence of the Zig-Zag Sampler

First, we would like to elucidate when the Zig-Zag sampler converges to the true posterior distribution. This is particularly important as we move beyond established means to simulate the process that are well studied and known to converge. There is a number of potential violations of the assumptions that guarantee convergence:

1. The surrogate model does not produce a strict upper bound process for the thinning.
2. We constantly change the offset γ to restore the upper bound property (although to a lesser extent at later times).
3. We constantly reduce the offset to recover from a potentially large gap between the surrogate and the true model.
4. We revert and redo events when the surrogate is found to be an invalid upper bound and the offset γ is increased.

We compare the following three scenarios to investigate the influence of these potential violations on performance and accuracy of the sampler:

- **Constant potential:** We use a constant surrogate model and increase the offset γ when needed. Additionally, the offset shrinks exponentially with time t . This tests points 2, 3, and 4.
- **Constant potential with no shrinkage:** We use a constant surrogate model and increase the offset γ when needed, but do not allow it to shrink. This tests points 2 and 4.
- **Random gradient:** We use a surrogate model that produces a random value for each iteration of the Zig-Zag sampler. We sample a value from $\mathcal{U}(-0.5, 0.5)$ for each component of the potential gradient. We increase the offset γ when needed, and allow it to shrink. This tests the limits of admitting a non-static upper bound process, i.e. tests points 1, 2.

The two constant surrogate models represent the most naive approach to surrogate modelling, where we simply use a constant value as an upper bound for the rate function. In theory, such a model would only be applicable to bounded domains, or a small number of distributions on unbounded domains, such as the Cauchy distribution. A Gaussian distribution, e.g. produces an unbounded rate function. In practice, however, all realizations of the Zig-Zag sampler are finite in time, and thus the rate function is bounded along any simulated trajectory. We would like to find this maximum value of the rate function with this constant model.

The random surrogate model represents a highly inaccurate model that does not provide much useful information about the rate function. Further, it is an extreme case of an ever-changing upper bound, which helps to isolate the influence of tampering with the upper bound process over time.

In Fig. 6, we compare the three scenarios in terms of the average RMSE of the posterior mean (top) and variance (bottom) estimates in $d = 2$, $d = 5$, and $d = 10$ dimensions. We also report the average ESS per model evaluation in Fig. 7. The first thing to point out is that all three scenarios converge to the true posterior distribution, as indicated by the RMSE of the posterior mean estimate in Figs. 6a to 6c. We can also observe convergence for the posterior variance in Figs. 6d to 6f, albeit with slight

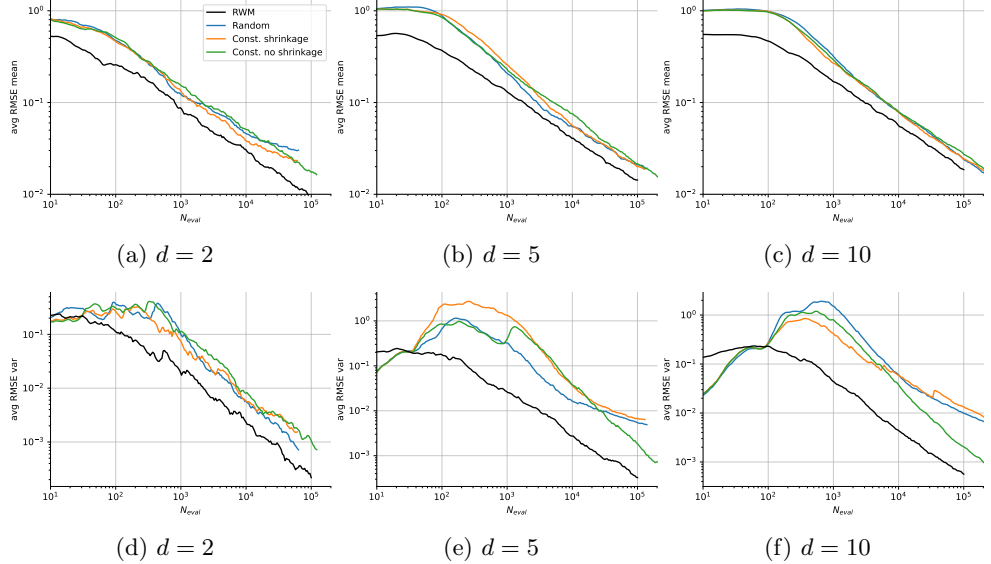


Fig. 6: RMSE of the mean (first row) and variance (second row) as functions of the number of model evaluations. All models converge, but perform worse than the baseline RWM sampler.

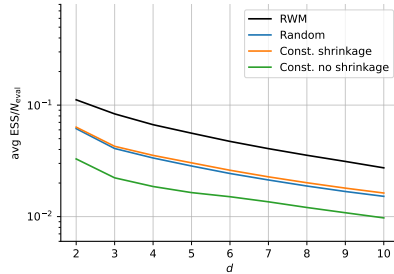


Fig. 7: Average ESS per model evaluation as a function of the dimensionality.

upward curvatures at later stages for the models with shrinkage. This is an important result, as it indicates that the Zig-Zag sampler is robust to the potential violations of the assumptions that guarantee convergence, and in line with [25], where a new upper bound is found for each event.

The second thing to note is the constant model with shrinkage performing best in terms of ESS per model evaluation, with a slight edge over the random model with shrinkage, as shown in Fig. 7. They both comfortably outperform the constant model without shrinkage in this metric. The frontrunner in the constant model is not surprising, as it should produce the tightest upper bound out of the three. The runner-up being the random model is less intuitive. This finding suggests two things: i)

While the randomness in the model might lead to an increase of the offset, it could by chance produce a tighter upper bound in regions of low process rate. ii) Shrinkage of the offset matters with such a naive surrogate model. More generally, we find that the influence of the shrinkage parameter β is less pronounced with better surrogate model accuracy, as discussed in detail in [A](#). The key takeaway from the analysis is that as long as the surrogate model is sufficiently accurate, the Zig-Zag sampler is robust to the choice of the shrinkage parameter.

Finally, it is obvious that the three models are not sufficiently accurate, as the Zig-Zag sampler is outperformed by the RWM sampler in terms of RMSE and ESS per model evaluation in all dimensions. This clearly illustrates the need for better surrogate models.

4.4 Surrogate Model Comparison

We now compare the performance of different surrogate models in terms of convergence rates and sampling efficiency. We consider the constant surrogate model, the Laplace approximation, and two Gaussian process surrogate models: one that observes only the function values, and one that additionally observes the gradients (Grad GP). Both GP models are trained with 25 points per latent space dimension. We set the shrinkage parameters to $\beta = 2 \times 10^{-2}$ for all simulations.

Figure 8 shows the average RMSE of the posterior mean (top row) and variance (bottom row) estimates for $d = 2$, $d = 5$, and $d = 10$ dimensions. With all surrogates except the constant model, the Zig-Zag sampler outperforms the RWM sampler across all metrics and dimensionalities. This even holds for the Laplace model, which is remarkable, as it is a rather crude approximation of the rate function. The rest of the models complete a consistent hierarchy, with the Grad GP performing best, followed by the GP, the Laplace, and finally the constant model. However, the Grad GP has the upper hand only by a small margin, suggesting that the additional information from the gradients is not crucial in these settings. In fact, the margin between the non-constant models shrinks with increasing dimensionality, indicating that the target distribution becomes more isotropic with finer discretizations of the underlying field.

Figure 9 shows the average ESS per model evaluation as a function of the dimensionality for all surrogate models. The ranking of the models is consistent with the RMSE results, with the Grad GP leading the field, followed by the GP, the Laplace, the RWM sampler, and finally the constant model.

4.5 Adaptive Refinement of the GP Surrogate Model

The last extension to the surrogate model is to adaptively refine the surrogate model during the PDMP simulation. Since we need to evaluate the model at each proposed event time, we can use the additional information from these points to update the surrogate model. We compare the pretrained GP surrogate model with an adaptive GP version (Ada GP) in [Fig. 10](#).

The Ada GP and GP curves fully overlap at the start of the simulation, as the Ada GP model is initialized with the same training data as the GP model. The adaptive refinement becomes apparent in later stages of the simulation, where the RMSE curves

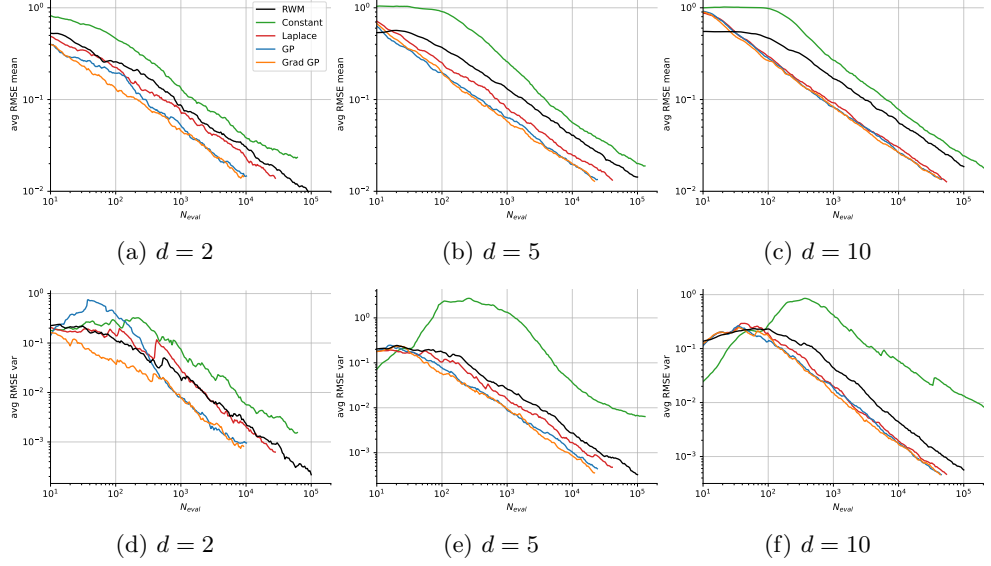


Fig. 8: Comparison of surrogate models in terms of RMSE of the mean (first row) and RMSE of the variance (second row). The more flexible Laplace, GP, and Grad GP models are accurate enough to outperform the RWM sampler.

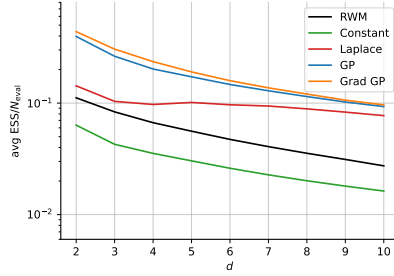


Fig. 9: Average ESS per model evaluation as a function of the dimensionality for all surrogate models. All but the constant surrogate outperform the RWM sampler.

of the two models become distinct. Counterintuitively, the Ada GP does not consistently outperform the GP model. In fact, the two curves cross multiple times in all three metrics. The ESS per model evaluation is slightly higher for the Ada GP model than for the GP models, but only by the smallest of margins, as shown in Fig. 11.

We hypothesize that the additional training points added during the simulation lie in regions well covered by the initial training set, and thus do not contribute much new information to the model. While the initial sampling from the Laplace approximation yields high-quality training points for this problem with moderate non-linearity, the situation may differ when strong non-linearities are present. We therefore assume that

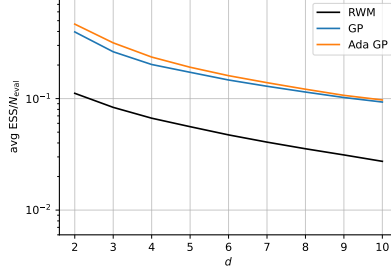


Fig. 11: Average ESS per model evaluation as a function of the dimensionality for the GP and Ada GP models.

the benefits of adaptive refinement are strongly problem-dependent, and that more sophisticated adaptive sampling strategies are required to fully leverage its potential in more challenging scenarios.

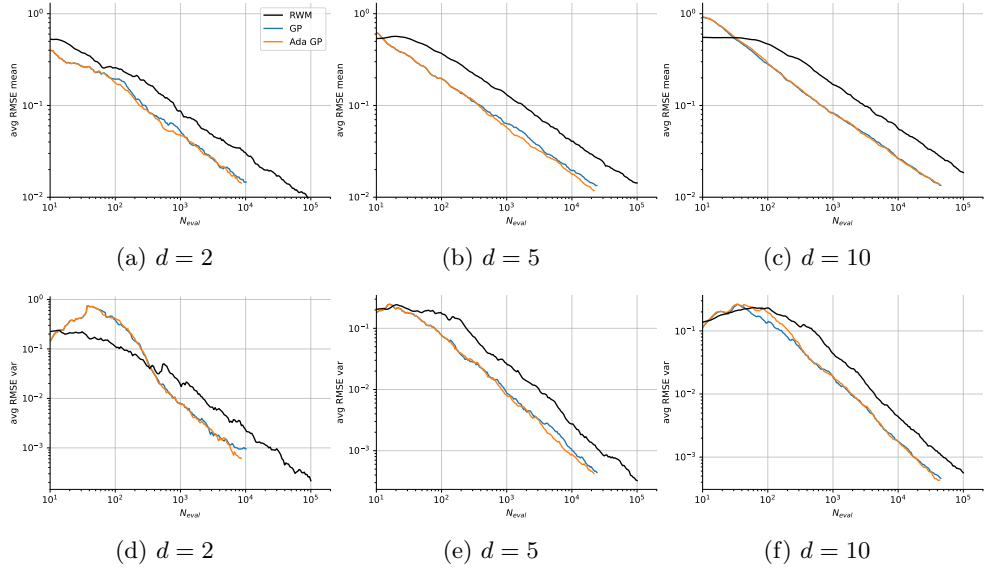


Fig. 10: Comparison of pretrained GP and Adaptive GP in terms of RMSE of the mean (first row) and RMSE of the variance (second row). The addition of more training points during the simulation does not consistently improve performance.

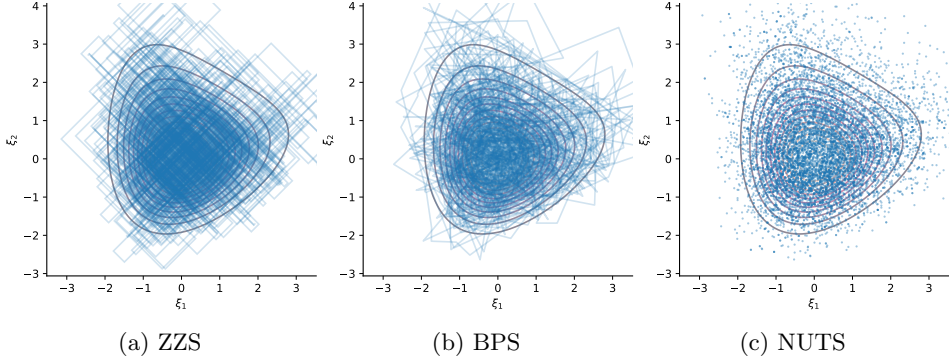


Fig. 12: Path of the (a) Zig-Zag sampler and (b) Bouncy Particle sampler, and (c) samples from the NUTS.

4.6 Zig-Zag Sampler vs Bouncy Particle Sampler vs No-U-Turn Sampler

Finally, we compare the performance of the Zig-Zag sampler with the Bouncy particle sampler and the NUTS. This comparison is necessary, as the latter is considered the state-of-the-art HMC algorithm for continuous distributions. For the Zig-Zag sampler and Bouncy particle sampler, we use the GP surrogate model with 25 points per latent space dimension. For NUTS, we use our own implementation of the algorithm with dual-averaging of the step size, as described in [7]. We cold-start the Zig-Zag sampler and the NUTS, i.e. we run them without any tweaking of the hyperparameters ahead of the inference. For Bouncy particle sampler, we use the refreshment rate deemed suitable in Section B, i.e. $\lambda_{\text{ref}} = 10^{-1}$. We show the paths of the Zig-Zag sampler, the Bouncy particle sampler, and the NUTS in Fig. 12.

The Bouncy particle sampler clearly outperforms the Zig-Zag sampler in terms of the posterior mean estimate, as shown in Figs. 13a to 13c. Both of the PDMP algorithms outperform the NUTS in all dimensions regarding this metric: Assuming a budget of 1000 model evaluations, both the Zig-Zag sampler and the Bouncy particle sampler achieve a RMSE of about 0.04, whereas the NUTS only reaches about 0.085 for $d = 2$. In $d = 10$ dimensions, the Bouncy particle sampler achieves a RMSE of about 0.04, whereas the NUTS is at 0.2, with the Zig-Zag sampler in between at about 0.08. The NUTS shows the worst performance in all dimensions, producing a RMSE of about 0.2.

A slightly different picture emerges when looking at the posterior variance estimates, as shown in Figs. 13d to 13f: Here, the Zig-Zag sampler outperforms both the Bouncy particle sampler and NUTS in all dimensions. The Bouncy particle sampler still outperforms the NUTS, but produces an equally accurate variance estimate as the RWM algorithm.

As no algorithm dominates across both metrics, we also consider the WD between the estimates from the different samplers and the reference solution. Inspecting the WD in Figs. 13g to 13i, we see that both PDMPs perform similarly well in $d = 2$ and $d = 5$ dimensions, with a slight edge for the Bouncy particle sampler in the $d = 10$

case. The NUTS again performs worst in all dimensions. However, it should be noted that the NUTS is structurally disadvantaged in this comparison: for a given budget of N_{eval} model evaluations it returns fewer posterior samples than the PDMP samplers (due to multiple leapfrog steps per accepted trajectory). The WD is thus computed from a smaller number of samples and exhibits a higher finite-sample bias.

A similar picture emerges when looking at the ESS per model evaluation, as shown in Fig. 14: The Bouncy particle sampler is leading the field, followed by the Zig-Zag sampler, and finally the NUTS. The NUTS only beats the RWM sampler for $d > 6$, thanks to its favorable scaling with dimensionality. The slope of the Zig-Zag sampler is similar to the one of the RWM algorithm. The Bouncy particle sampler, however, displays a slope closer to the one of the NUTS, albeit with a higher offset, suggesting better scaling with dimensionality than the Zig-Zag sampler.

At a first glance, the weak performance of the NUTS sampler in this comparison is surprising, given its reputation as a state-of-the-art MCMC algorithm. There are several possible explanations for this outcome: i) The affine transformation leads to a more isotropic distribution, which improves the performance of the Zig-Zag sampler and the RWM algorithm relative to the NUTS. ii) The distribution only shows moderate non-linearities. iii) The cold-start of the NUTS sampler leads to suboptimal hyperparameters, which hamper its performance. In many practical applications, users would invest $> 10^3$ iterations in tuning the hyperparameters of NUTS ahead of the actual inference. When expensive PDE model evaluations are involved, such an upfront investment is typically not feasible. Simply put, the NUTS does not excel in the settings considered here, even though it does in many others.

5 Conclusions

In this work, we introduced and analyzed a surrogate-assisted framework for simulating piecewise-deterministic Markov process (PDMP) samplers in non-linear Bayesian inverse problems governed by partial differential equations (PDEs). Focusing on the Zig-Zag sampler (Zig-Zag sampler) and the Bouncy Particle sampler (Bouncy particle sampler), we designed a global thinning strategy that uses a surrogate for the potential together with a simple, yet effective, correction mechanism for the resulting event rate. This construction makes the method agnostic to the particular surrogate family: whenever the surrogate underestimates the true rate locally, the offset is increased to restore the upper-bound property required for valid thinning.

Our numerical experiments—the inference of a coefficient field in linear elasticity—demonstrated that this approach yields PDMP samplers that were both robust and efficient. Even very crude surrogates, such as a constant model or a pure Laplace approximation in whitened coordinates, can be corrected on the fly and were empirically observed to converge to the reference posterior. More expressive Gaussian process (GP) surrogates on top of the Laplace approximation further tightened the rate approximation and improved sampling efficiency across the board. While the Gaussian process model offered clear benefits, incorporating derivative observations and adaptive refinement yielded only modest additional gains in performance for our benchmark problem.

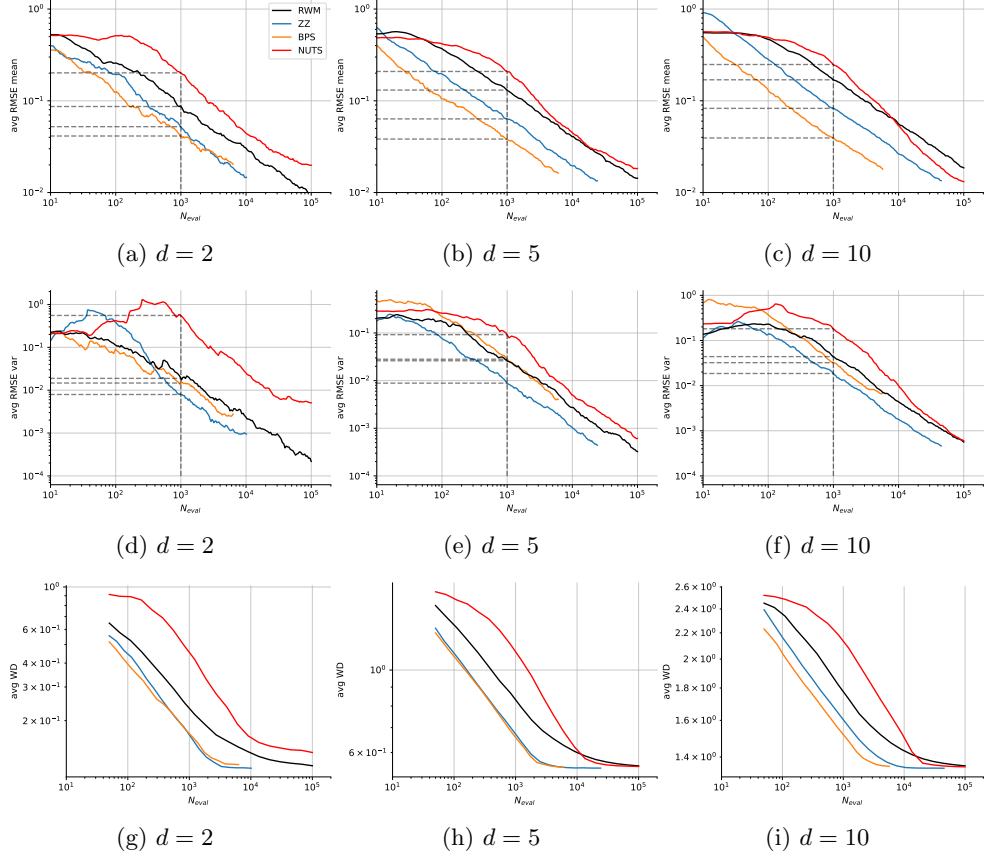


Fig. 13: Comparison of Zig-Zag sampler, Bouncy particle sampler, and NUTS in terms of RMSE of the mean (top row), RMSE of the variance (middle row), and WD (bottom row). Both PDMPs outperform the NUTS in all dimensions regarding the posterior mean and variance estimates and the WD.

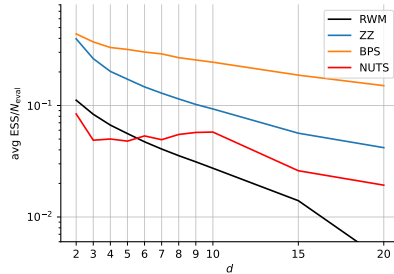


Fig. 14: Average ESS per model evaluation as a function of the dimensionality for Zig-Zag sampler, Bouncy particle sampler, NUTS, and RWM. The Bouncy particle sampler is the most efficient sampler, followed by the Zig-Zag sampler, NUTS, and RWM.

We concluded with a comparison of the Zig-Zag sampler and the Bouncy particle sampler within the surrogate-assisted framework. The Bouncy particle sampler had the upper hand regarding the posterior mean estimation error, the Zig-Zag sampler attained better performance in terms of variance estimation, and both algorithms were largely on par regarding the Wasserstein distance. The Bouncy particle sampler exhibited a higher effective sample size per model evaluation, particularly evident in higher dimensions. Both PDMP samplers outperformed a well tuned Random Walk Metropolis baseline and the popular No-U-Turn Sampler in all considered metrics, across all settings.

This study was restricted to smooth, unimodal posteriors arising from an elliptic PDE with an analytic forward map and moderate parameter dimensions. A limitation of the employed Gaussian process surrogates is their cubic training cost in the number of design points, which limits their applicability in very high dimensions. Moreover, while our empirical evidence supported convergence of the surrogate-assisted PDMP samplers under the proposed correction scheme, a theoretical analysis of convergence for adaptive and non-strict upper bounds remains an open problem.

Future research directions include extending the approach to more realistic PDE-governed inverse problems, higher-dimensional parameter spaces, and possibly multimodal posteriors. On the surrogate side, sparse or low-rank Gaussian process constructions or neural surrogates could alleviate the cubic scaling while preserving global accuracy. Finally, a rigorous theoretical treatment of convergence properties for the proposed surrogate-assisted PDMP samplers would provide valuable insights and guidance for practical applications. Nevertheless, this work establishes the first successful application of PDMP sampling to PDE-governed Bayesian inverse problems, demonstrating their viability for a wide range of scientific and engineering applications.

CRediT Authorship Contribution Statement. L. Riccius: Conceptualization, Methodology, Software, Validation, Investigation, Visualization, Writing - Original Draft. I.B.C.M. Rocha: Conceptualization, Methodology, Supervision, Writing - Review & Editing. J. Bierkens: Methodology, Writing - Review & Editing. H. Kekkonen: Writing - Review & Editing. F.P. van der Meer: Conceptualization, Methodology, Supervision, Writing - Review & Editing.

Acknowledgements. This work is supported by the TU Delft AI Labs programme through the SLIMM lab.

Code Availability. The code used in this study is available at github.com/SLIMM-Lab/pdmp.git.

Appendix A Influence of the Shrinkage Parameter β

For completeness, we investigate the influence of the shrinkage parameter β in Eq. (26) on the performance of the Zig-Zag sampler with different surrogate models. We include the constant surrogate model, a Laplace approximation, and two Gaussian process surrogate models with 25 and 100 training points per latent space dimension, respectively. For each surrogate model—represented by a row in Fig. A1—we report the average RMSE of the posterior mean estimate across a range of shrinkage parameter

values β . The experiments are conducted in $d = 2$, $d = 5$, and $d = 10$ dimensions and shown as the columns of Fig. A1.

As a first observation, the Zig-Zag sampler converges with all surrogate models when the shrinkage parameter is sufficiently small, i.e., $\beta \leq 2 \times 10^{-2}$. A second observation is that the Zig-Zag sampler converges for all β values when using GP surrogate models, which are the most flexible in approximating the rate function. For the Laplace model, the Zig-Zag sampler fails to converge for $\beta \geq 2$. In these cases, the RMSE stagnates after a few hundred model evaluations, pointing to a persistent model bias. The constant surrogate model performs worst. It not only fails to converge for $\beta \leq 2 \times 10^{-2}$ for all dimensionalities, but in fact diverges. Results for $\beta \geq 2 \times 10^{-2}$ are omitted, as the PDMP simulation terminated prematurely for all random seeds due to numerical issues caused by large offset values.

To better understand the failure of the constant surrogate with large shrinkage parameters, we inspect the trajectories of the Zig-Zag sampler. We consider a representative realization of the two-dimensional case with $\beta = 2 \times 10^{-1}$. After an initial phase of expected behaviour, during which the sampler explores the high-density region of the distribution, it suddenly drifts toward the lower-left corner of the domain, as shown in Fig. A2a. The close-up in Fig. A2b reveals that the sampler oscillates around a line of points with zero gradient in the ξ_1 direction, while steadily moving in the negative ξ_2 direction. Fig. A2c illustrates the time interval just before and after this departure: both velocity components flip regularly until about $t = 50$, after which v_2 remains fixed at -1 , while v_1 continues flipping at an increasing rate.

This behaviour can be traced to the offset dynamics. The large offset in the v_1 component drives frequent events, but the smaller offset in the v_2 component quickly shrinks to zero for larger β . At the same time, the offset in the v_1 component continues to grow, as we move further away from the high-density region. As a result, the proposal mechanism fails to generate events in the v_2 direction, causing the sampler to drift downward without correction. Since the offset is only updated after an event in the corresponding direction and such an event never occurs, the sampler diverges.

When the shrinkage parameter is sufficiently small, the PDMP spends an initial phase adjusting to an appropriate offset value, visible as a plateau at the start of the RMSE curves in Figs. A1a to A1c. Once this value is established, it remains largely stable with only minor decreases over time, allowing the sampler to slowly converge. For the more accurate and therefore more robust GP surrogates, runs with large values of β also converge. In these cases, it appears beneficial that the offset recovers quickly after an unlikely event in the distribution's tail, which forces a jump in the offset.

Appendix B Bouncy Particle Sampler Refreshment Rate

Before we can put the Bouncy particle sampler to the test, we need to determine a suitable refreshment rate λ_{ref} , which determines how often the velocity is resampled from its prior distribution. A high refreshment rate leads to more frequent updates of this kind, which ensures ergodicity of the sampler. However, it also makes the process more diffusive, more akin to a random walk, and thus less efficient. The optimal

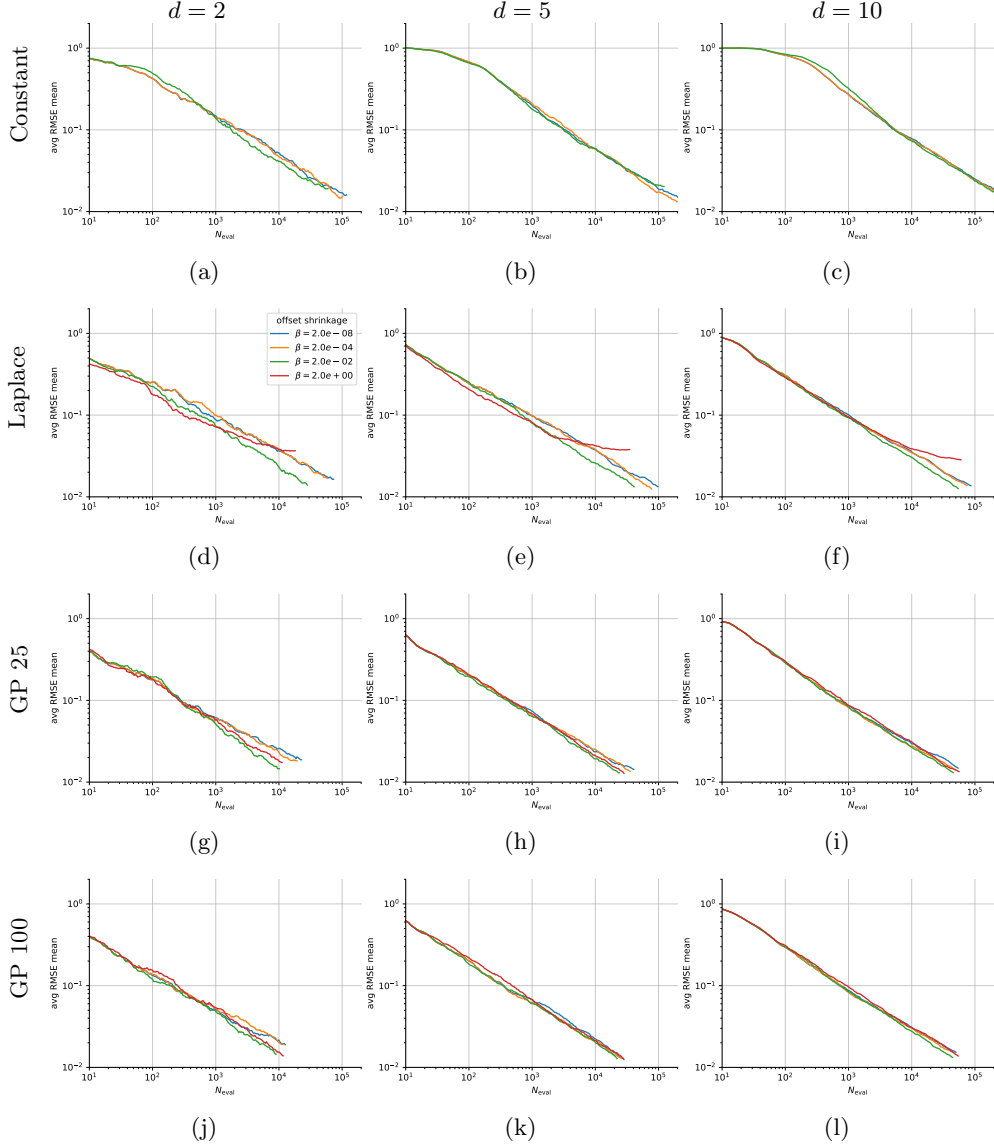


Fig. A1: Average RMSE of the posterior mean estimate as a function of the number of model evaluations for different shrinkage parameters and surrogate models.

refreshment rate is therefore a compromise between these two effects. We investigate the influence of the refreshment rate on the performance of the Bouncy particle sampler with a GP surrogate model with 25 points per latent space dimension. We consider refreshment rates $\lambda_{\text{ref}} \in \{10^{-3}, 10^{-2}, 10^{-1}, 1\}$.

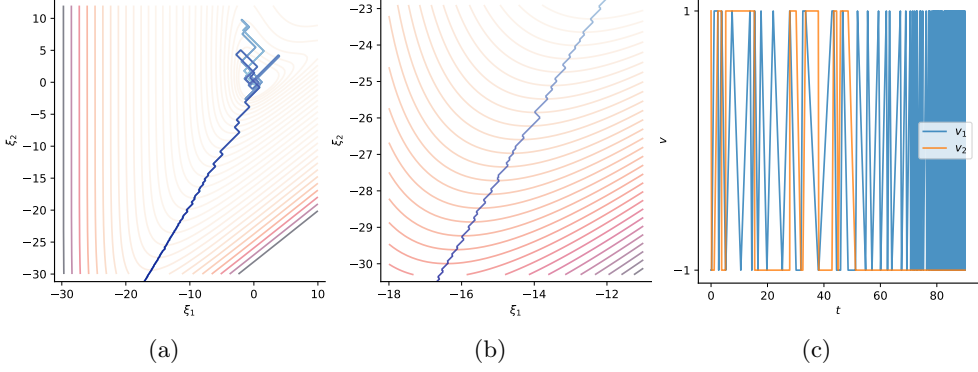


Fig. A2: Inspection of Zig-Zag sampler's path for the constant surrogate model with shrinkage parameter $\beta = 2 \cdot 10^{-1}$. (a) Path and log-density. (b) Behaviour of the sampler in the tail. (c) Velocities of the sampler. The time is indicated by the colour gradient from light to dark in (a) and (b).

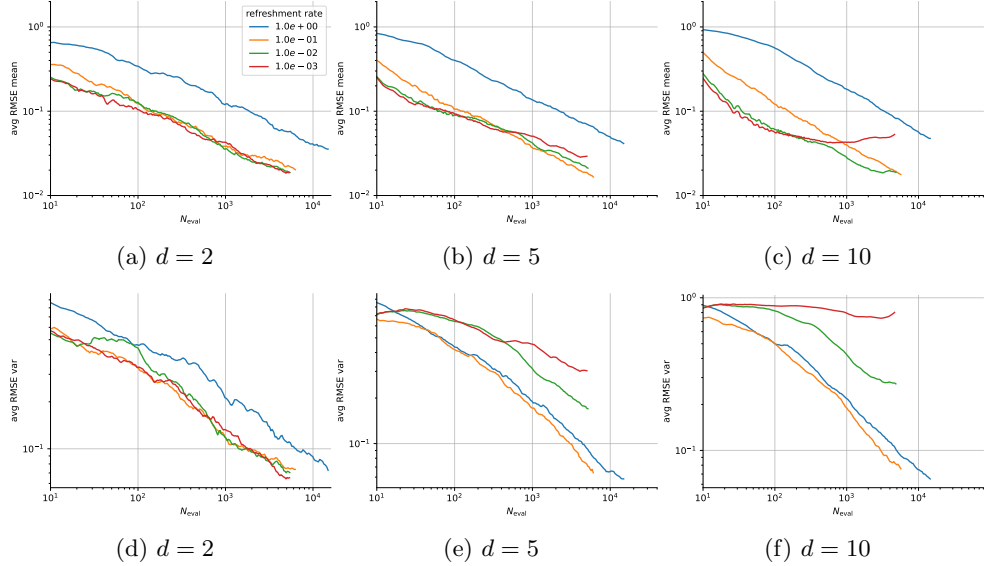


Fig. B3: Comparison of different Bouncy particle sampler refreshment rates in terms of RMSE of the mean (top row) and variance (bottom row). Moderate refreshment rates yield the best performance across both metrics.

The results in Fig. B3 show that the refreshment rate has a noticeable influence on the performance of the Bouncy particle sampler. High refreshment rates lead to slower convergence in terms of the posterior mean estimate in the top row of Fig. B3. The performance in terms of accuracy of the mean is relatively stable for $\lambda_{\text{ref}} \leq 10^{-1}$,

suggesting diminishing returns for lower refreshment rates. A look at the variance in the bottom row of Fig. B3, however, reveals a different picture: very low refreshment rates lead to poor approximation of the posterior variance, suggesting the ergodicity of the sampler is compromised in the absence of refreshments. We see that setting the refreshment rate too high leads to slow exploration, and choosing it too low to poor coverage, but there seems to be a sweet spot around $\lambda_{\text{ref}} = 10^{-1}$.

References

- [1] Metropolis, N., Rosenbluth, A.W., Rosenbluth, M.N., Teller, A.H., Teller, E.: Equation of state calculations by fast computing machines. *The Journal of Chemical Physics* **21**, 1087–1092 (1953) <https://doi.org/10.1063/1.1699114>
- [2] Hastings, W.K.: Monte carlo sampling methods using markov chains and their applications. *Biometrika* **57**, 97 (1970) <https://doi.org/10.2307/2334940>
- [3] Roberts, G.O., Rosenthal, J.S.: Optimal scaling for various metropolis-hastings algorithms. <https://doi.org/10.1214/ss/1015346320> **16**, 351–367 (2001) <https://doi.org/10.1214/SS/1015346320>
- [4] Roberts, G.O., Stramer, O.: Langevin diffusions and metropolis-hastings algorithms. *Methodology And Computing In Applied Probability* 2002 4:4 **4**, 337–357 (2002) <https://doi.org/10.1023/A:1023562417138>
- [5] Duane, S., Kennedy, A.D., Pendleton, B.J., Roweth, D.: Hybrid monte carlo. *Physics Letters B* **195**, 216–222 (1987) [https://doi.org/10.1016/0370-2693\(87\)91197-X](https://doi.org/10.1016/0370-2693(87)91197-X)
- [6] Girolami, M., Calderhead, B.: Riemann manifold langevin and hamiltonian monte carlo methods. *Journal of the Royal Statistical Society. Series B: Statistical Methodology* **73**, 123–214 (2011) <https://doi.org/10.1111/j.1467-9868.2010.00765.x>
- [7] Hoffman, M.D., Gelman, A.: The no-u-turn sampler: Adaptively setting path lengths in hamiltonian monte carlo. *Journal of Machine Learning Research* **15**, 1593–1623 (2014)
- [8] Carpenter, B., Gelman, A., Hoffman, M.D., Lee, D., Goodrich, B., Betancourt, M., Brubaker, M., Guo, J., Li, P., Riddell, A.: Stan: A probabilistic programming language. *Journal of Statistical Software* **76** (2017) <https://doi.org/10.18637/jss.v076.i01>
- [9] Salvatier, J., Wiecki, T.V., Fonnesbeck, C.: Probabilistic programming in python using pymc3. *PeerJ Computer Science* **2**, 55 (2016) <https://doi.org/10.7717/peerj-cs.55>

- [10] Chong, A., Lam, K.P.: A comparison of mcmc algorithms for the bayesian calibration of building energy models for building simulation 2017 conference. In: Building Simulation Conference Proceedings, vol. 2, pp. 582–591 (2017). <https://doi.org/10.26868/25222708.2017.336> . <https://doi.org/10.26868/25222708.2017.336>
- [11] Goodman, J., Weare, J.: Ensemble samplers with affine invariance. *Communications in Applied Mathematics and Computational Science* **5**, 65–80 (2010) <https://doi.org/10.2140/camcos.2010.5.65>
- [12] Gelman, A., Gilks, W.R., Roberts, G.O.: Weak convergence and optimal scaling of random walk metropolis algorithms. *The Annals of Applied Probability* **7**, 110–120 (1997) <https://doi.org/10.1214/aoap/1034625254>
- [13] Roberts, G.O., Rosenthal, J.S.: Optimal scaling of discrete approximations to langevin diffusions. *Journal of the Royal Statistical Society Series B: Statistical Methodology* **60**, 255–268 (1998) <https://doi.org/10.1111/1467-9868.00123>
- [14] Grimmett, G., Stirzaker, D.: Probability and Random Processes, 4th edn. Oxford University Press, Oxford (2016). <https://academic.oup.com/book/52807>
- [15] Chen, T.-L., Hwang, C.-R.: Accelerating reversible markov chains. *Statistics and Probability Letters* **83**, 1956–1962 (2013) <https://doi.org/10.1016/j.spl.2013.05.002>
- [16] Bierkens, J.: Non-reversible metropolis-hastings. *Statistics and Computing* **26**, 1213–1228 (2016) <https://doi.org/10.1007/S11222-015-9598-X/TABLES/2>
- [17] Ma, Y.-A., Fox, E.B., Chen, T., Wu, L.: A unifying framework for devising efficient and irreversible mcmc samplers (2016)
- [18] Bierkens, J., Roberts, G.: A piecewise deterministic scaling limit of lifted metropolis–hastings in the curie–weiss model. *The Annals of Applied Probability* **27**, 846–882 (2017) <https://doi.org/10.1214/16-AAP1217>
- [19] Bouchard-Côté, A., Vollmer, S.J., Doucet, A.: The bouncy particle sampler: A nonreversible rejection-free markov chain monte carlo method. *Journal of the American Statistical Association* **113**, 855–867 (2018) <https://doi.org/10.1080/01621459.2017.1294075>
- [20] Bierkens, J., Grazzi, S., Kamatani, K., Roberts, G.: The boomerang sampler. In: Daumé, A.H., Singh (eds.) *Proceedings of the 37th International Conference on Machine Learning*, pp. 908–918. PMLR, Vienna (2020). <https://proceedings.mlr.press/v119/bierkens20a.html>
- [21] Bierkens, J., Fearnhead, P., Roberts, G.: The zig-zag process and super-efficient sampling for bayesian analysis of big data. *The Annals of Statistics* **47**, 1288–1320 (2019) <https://doi.org/10.1214/18-AOS1715>

- [22] Ke, X., Fan, Y., Zhou, Q.: Fused $L_{1/2}$ prior for large scale linear inverse problem with gibbs bouncy particle sampler (2025)
- [23] Bertazzi, A., Bierkens, J.: Adaptive schemes for piecewise deterministic monte carlo algorithms. *Bernoulli* **28** (2022) <https://doi.org/10.3150/21-BEJ1423>
- [24] Pagani, F., Chevallier, A., Power, S., House, T., Cotter, S.: Nuzz: Numerical zig-zag for general models. *Statistics and Computing* **34**, 1–26 (2024) <https://doi.org/10.1007/S11222-023-10363-8/FIGURES/2>
- [25] Corbella, A., Spencer, S.E.F., Roberts, G.O.: Automatic zig-zag sampling in practice. *Statistics and Computing* **32**, 1–16 (2022)
- [26] Fearnhead, P., Bierkens, J., Pollock, M., Roberts, G.O.: Piecewise deterministic markov processes for continuous-time monte carlo. *Statistical Science* **33**, 386–412 (2018) <https://doi.org/10.1214/18-STS648>
- [27] Bierkens, J., Roberts, G.O., Zitt, P.-A.: Ergodicity of the zigzag process. *The Annals of Applied Probability* **29**, 2266–2301 (2019) <https://doi.org/10.1214/18-AAP1453>
- [28] Peters, E.A.J.F., With, G.D.: Rejection-free monte carlo sampling for general potentials. *Physical Review E - Statistical, Nonlinear, and Soft Matter Physics* **85**, 026703 (2012) <https://doi.org/10.1103/PHYSREVE.85.026703/FIGURES/5/MEDIUM>
- [29] Bierkens, J., Kamatani, K., Roberts, G.O.: Scaling of piecewise deterministic monte carlo for anisotropic targets. *Bernoulli* **31** (2025) <https://doi.org/10.3150/24-BEJ1807>
- [30] Lewis, P.A.W., Shedler, G.S.: Simulation of nonhomogeneous poisson processes by thinning. *Naval Research Logistics Quarterly* **26**, 403–413 (1979) <https://doi.org/10.1002/NAV.3800260304>
- [31] Kennedy, M.C., O'Hagan, A.: Bayesian calibration of computer models. *Journal of the Royal Statistical Society. Series B: Statistical Methodology* **63**, 425–464 (2001) <https://doi.org/10.1111/1467-9868.00294>
- [32] Riccius, L., Rocha, I.B.C.M., Bierkens, J., Kekkonen, H., Meer, F.P.: Integration of active learning and mcmc sampling for efficient bayesian calibration of mechanical properties. *European Journal of Mechanics - A/Solids*, 106015 (2026) <https://doi.org/10.1016/J.EUROMECHSOL.2026.106015>
- [33] Feydy, J., Séjourné, T., Vialard, F.X., Amari, S.I., Trouvé, A., Peyré, G.: Interpolating between optimal transport and mmd using sinkhorn divergences. *AISTATS 2019 - 22nd International Conference on Artificial Intelligence and Statistics* (2018)

[34] Andrieu, C., Thoms, J.: A tutorial on adaptive mcmc. *Statistics and Computing* **18**, 343–373 (2008) <https://doi.org/10.1007/s11222-008-9110-y>